NEUROSCIENCE

Membrane-associated Rhes-Slc4a7 complex orchestrates tunneling nanotube formation and mutant Huntingtin spread

Sunayana Dagar[1,2,3], Alexandra Fernandez[4], Uri Nimrod Ramírez-Jarquín[5], Violeta Gisselle Lopez-Huerta[6], Emaad Mirza[4], Chinmayee Mohapatra[1,2,3], Isabella Zuniga[4], Nicolai T. Urban[7], Gogce Crynen[8], George Tsaprailis[9], Srinivasa Subramaniam[1,2,3,10]*

Tunneling nanotubes (TNTs) are membranous structures that mediate intercellular transfer of proteins, including the pathogenic mutant Huntingtin (mHTT) protein in Huntington disease (HD). We previously identified the ras homolog enriched in the striatum (Rhes) as a key regulator of TNT formation and mHTT transmission; however, the molecular components underlying this process remained unknown. Here, using unbiased liquid chromatography–tandem mass spectrometry analysis of membrane-associated Rhes complexes, we identify Slc4a7 (solute carrier family 4 member 7), an intracellular pH sensor, as a top membrane-binding partner of Rhes. Functional studies revealed that small interfering RNA–mediated depletion or pharmacological inhibition of Slc4a7 substantially reduced Rhes-induced TNT formation and suppressed mHTT intercellular transfer. Mechanistically, Rhes directly interacts with Slc4a7 through both its amino- and carboxyl-terminal domains and modulates intracellular pH to facilitate TNT formation. This interaction does not depend on the transporter activity of Slc4a7. However, inhibition of Rhes farnesylation—a lipid modification that anchors Rhes to the membrane—disrupts its binding to Slc4a7 and abolishes TNT formation. Slc4a7 knock-out mice showed markedly reduced cell-to-cell transmission of mHTT in the striatum in vivo. Together, these findings uncover a previously unrecognized Rhes-Slc4a7 signaling axis critical for TNT-mediated mHTT transmission and highlight Slc4a7 as a potential therapeutic target to limit disease spread in HD.

INTRODUCTION

Intercellular communication in the brain is essential for maintaining neural function and responding to injury or disease. One emerging mode of such communication is through tunneling nanotubes (TNTs)—thin, actin-based membranous structures that form direct cytoplasmic bridges between cells (*1*). TNTs have gathered increasing attention for their role in the intercellular transfer of proteins, vesicles, and even organelles, particularly in the context of neurodegeneration (*2*–*7*). However, the precise molecular regulators of TNT formation and their physiological relevance in the brain remain poorly understood.

Ras homolog enriched in the striatum (Rhes), an atypical guanosine triphosphatase (GTPase) with small ubiquitin–like modifier (SUMO) E3–like activity, enriched in striatal neurons that we recently identified as a key mediator of TNT-like protrusions between neuronal cells (*8*, *9*). We showed that Rhes (*Rasd2*) induces the biogenesis of actin-dependent TNT-like structures—termed "Rhes tunnels"—and facilitates the transport of the mutant Huntingtin (mHTT) protein between neuronal cells (*10*). This process is dependent on the structural integrity of Rhes, including its CAAX motif and SUMO E3–like domain, highlighting a membrane binding and SUMOylation-dependent mechanism of cargo transfer (*10*).

In our subsequent in vivo studies, we have confirmed that Rhes moves between neurons in the striatum and extends to cortical regions, thereby enabling long-range transport of mHTT in the mouse brain (*11*). We found that the deletion of Rhes diminishes this intercellular spread, suggesting a crucial role in disease propagation in the striatum (*11*). These findings have been further supported by imaging and molecular studies in striatal slices and organotypic cultures, confirming Rhes-mediated TNTs as a likely route for protein transmission in the intact brain (*11*). Despite these studies, the molecular mechanisms by which Rhes promotes TNT formation remained unclear.

Solute carrier family 4 member 7 (Slc4a7) encodes NBCn1, an electroneutral sodium bicarbonate cotransporter that is critical for maintaining intracellular pH homeostasis—particularly in environments with high metabolic or signaling demand (*12*, *13*). While Slc4a7 has been well studied in epithelial tissues, its role in the brain is becoming increasingly appreciated. In neurons, Slc4a7 helps regulate neuronal excitability and hearing function (*14*), and its deletion has been shown to impair locomotor activity and alter exploratory behavior in mice (*14*). Slc4a7 also contributes to retinal development (*15*) and has been implicated in coordinating intracellular pH during cell proliferation and migration (*16*). Through unbiased liquid chromatography–tandem mass spectrometry (LC-MS/MS) protein interaction analysis, we identified Slc4a7 as a prominent interactor of Rhes and demonstrate its functional role in regulating Rhes-mediated TNT formation and mHTT transmission as described below.

[1]Department of Chemistry/Biochemistry, Florida Atlantic University, Boca Raton, FL 33431, USA. [2]Stiles-Nicholson Brain Institute, FAU, Jupiter, FL 33458, USA. [3]David and Lynn Nicholson Center for Neuroscience Research, Jupiter, FL 33458, USA. [4]Harriet L. Wilkes Honors College, FAU, Jupiter, FL 33458, USA. [5]Facultad de Ciencias, National Autonomous University of Mexico, Ciudad de México 04510, Mexico. [6]Institute of Cellular Physiology, National Autonomous University of Mexico, Mexico City 04510, Mexico. [7]Max Planck Institute for Neuroscience, ZEISS Microscopy Solutions Center, Jupiter, FL 33458, USA. [8]Bioinformatics and Statistics Core, The Herbert Wertheim UF Scripps Institute for Biomedical Innovation and Technology, Jupiter, FL 33458, USA. [9]Mass Spectrometry and Proteomics core, The Herbert Wertheim UF Scripps Institute for Biomedical Innovation and Technology, Jupiter, FL 33458, USA. [10]Center for Molecular Biology and Biotechnology, FAU, Jupiter, FL 33458.
*Corresponding author. Email: ssubramaniam@fau.edu

RESULTS

Membrane-anchored Rhes drives formation of open-ended TNT between cells

To assess the role of Rhes in TNT formation across diverse cell types, we generated stable cell lines expressing green fluorescent protein (EGFP) or EGFP-Rhes WT using lentiviral vectors in mouse striatal neuronal cells and used targeted integration into the Citrate Lyase Beta-Like (CLYBL) genomic safe harbor locus (*17*) to establish stable EGFP or EGFP-Rhes WT expression in human SH-SY5Y neuroblastoma cells and HD human induced pluripotent stem cells (iPSCs). In all models, GFP-Rhes strongly induced TNT-like structures (~fourfold versus GFP alone), suggesting a conserved function of Rhes in promoting intercellular connectivity (Fig. 1, A and B). These TNT-like structures were suspended above the substratum and clearly connected two cells, with lengths ranging from 15 to 25 μm and diameters of 200 to 300 nm (fig. S1, A to C). In addition, we examined the function of endogenous RASD2 in U-87 glioblastoma cells, which naturally express *RASD2*, to further assess its role in TNT formation using phalloidin staining to visualize actin-based structures (Fig. 1C). Small interfering RNA (siRNA)–mediated depletion of *RASD2* in U-87 cells significantly reduced the number of TNTs, further confirming its essential role in TNT biogenesis (Fig. 1, D and E). The average length and diameter of TNTs in U-87 cells were approximately 10 μm and 200 nm, respectively, and were unaffected by RASD2 depletion (fig. S1, D and E). Conversely, overexpression of Rhes WT, but not the C263S mutant (defective in membrane binding), in U-87 cells induced numerous TNT formation (Fig. 1, F and G), increasing their average length from approximately 10 μm in control cells to 30 μm, while the diameters remained unaffected (fig. S1, F and G). Notably, the expression levels of EGFP-Rhes WT and EGFP-Rhes-C263S were comparable (Fig. 1, H and I), with no detectable impact on cell viability under either condition (fig. S1H). Together, these results demonstrate that Rhes promotes TNT formation in a broad range of cell types, both through endogenous regulation and overexpression via membrane binding.

Live-cell imaging analysis reveal cargo (for example, lysosome and endosome) in Rhes-TNTs travel along the plasma membrane before delivery into the acceptor cells (*8*, *10*). However, whether Rhes-TNTs are closed-ended or open-ended is unclear. To determine this, we used the split-GFP system (*18*) as a functional readout for cytoplasmic continuity between donor and acceptor cells (Fig. 2A). In this system, donor cells expressed G10–internal ribosomal entry site (IRES)–mCherry (GFP10), whereas acceptor cells expressed CD63-7G11-IRES–cyan fluorescent protein (CFP, or GFP11). Before coculture, the individual cells exhibited no GFP fluorescence (day 1, Fig. 2B), confirming that the split-GFP fragments alone are nonfunctional when separated. However, upon coculture and fluorescence-activated cell sorting (FACS) in the presence of Rhes (day 2), a strong GFP signal was reconstituted in (CFP^+) acceptor cells (Fig. 2, C and D), indicating that Rhes facilitates the transfer of GFP10-tagged vesicular components through TNT-like structures and enables their proximity to GFP11 in recipient cells (Fig. 2E). Although this assay provides strong evidence that Rhes promotes TNT-mediated intercellular transport in an open-ended manner, the possibility that TNTs are initially close-ended and become open-ended upon fusion with the acceptor cell cannot be ruled out as the underlying mechanisms remain unclear.

Slc4a7 identified as a key membrane interactor of Rhes

To understand the mechanism by which Rhes promotes TNTs, we leveraged its known requirement to interact with membrane component. As shown in Fig. 3, A and B, a membrane–targeting–deficient mutant of Rhes failed to promote TNT formation, suggesting that membrane-associated components play a critical role in this process. On the basis of this observation, we hypothesized that Rhes interacts with specific membrane-associated proteins that are essential for initiating or stabilizing TNTs. To test this, we set out to identify membrane-bound targets that physically associate with Rhes and potentially mediate its role in TNT formation.

To identify membrane-associated protein interactors of Rhes, we transfected striatal neuronal cells with EGFP, EGFP-Rhes WT, or EGFP-Rhes C263S (a membrane binding–deficient mutant) and then performed biochemical membrane fractionation (Fig. 3B). Membrane fractions were subjected to immunoprecipitation (IP) using anti-GFP nanobody–conjugated magnetic beads to selectively isolate GFP-tagged proteins.. The IP bead-bound complexes were then subjected to LC-MS/MS analysis to uncover proteins interacting with membrane-associated Rhes (Fig. 3B).

This proteomics approach identified 188 proteins that were reproducibly enriched in at least two of three independent GFP-nanobody immunoprecipitation replicates from the EGFP-Rhes WT samples but absent in both EGFP-only and EGFP-Rhes C263S control samples, indicating specific interaction with membrane-anchored Rhes (Fig. 3C and data sheet 1). All identified proteins met stringent selection criteria, including a minimum of two unique peptides per protein and a protein-level false discovery rate (FDR) of ≤1%.

Pathway analysis of the 188 Rhes WT–specific membrane interactorsusing STRING (Fig. 3D) and Gene Ontology enrichment revealed significant association with biological processes such as macroautophagy, autophagy, and metabolic processes (FDR ≤ 0.0125) (Fig. 3E). Molecular function terms included Hsp90 (FDR ~ 0.0302), cellular component analysis indicated strong enrichment for cytoplasmic and organelle-localized proteins (FDR ≤ 1.68×10^{-11}), suggesting that membrane-anchored Rhes interacts with proteins involved in trafficking, stress response, and degradation pathways (Fig. 3E).

Among the top 10 Rhes WT–specific membrane interactors identified through proteomic analysis, Slc4a7, an anion exchange bicarbonate transporter involved in pH regulation emerged as a prominent candidate (Fig. 4A). Its strong and specific enrichment in Rhes WT—but not in GFP or Rhes C263S samples (fig. S2)—suggests a direct or indirect association with membrane-anchored Rhes, pointing to a potential role in mediating Rhes-driven intercellular communication or trafficking processes.

Slc4a7 mediates Rhes-induced TNT formation

To assess the functional relevance of Rhes-associated membrane interactors in TNT formation, we performed candidate-based siRNA screening of selected targets (Fig. 4A). Among these, siRNA against Slc4a7, Plastin-2, WIPI-2, Twinfilin-2, and PKP4, significantly reduced the number of Rhes-mediated TNTs (Fig. 4B). Plastin-2 (*19*), Twinfilin-2 (*20*), and PKP4 (*21*) are cytoskeletal regulators involved in maintaining cell structure, motility, and adhesion. These proteins contribute to the dynamic remodeling of the actin network, which is essential for processes such as membrane protrusion and intercellular connectivity (*22*). Although their role in TNT formation has not been established, their involvement is plausible given that actin polymerization is essential for Rhes-induced TNTs (*10*).

We focused on Slc4a7, as its role in TNT biology has not been previously reported. Supporting the siRNA results, Slc4a7 knockdown markedly suppressed Rhes-mediated TNT formation (Fig. 4,

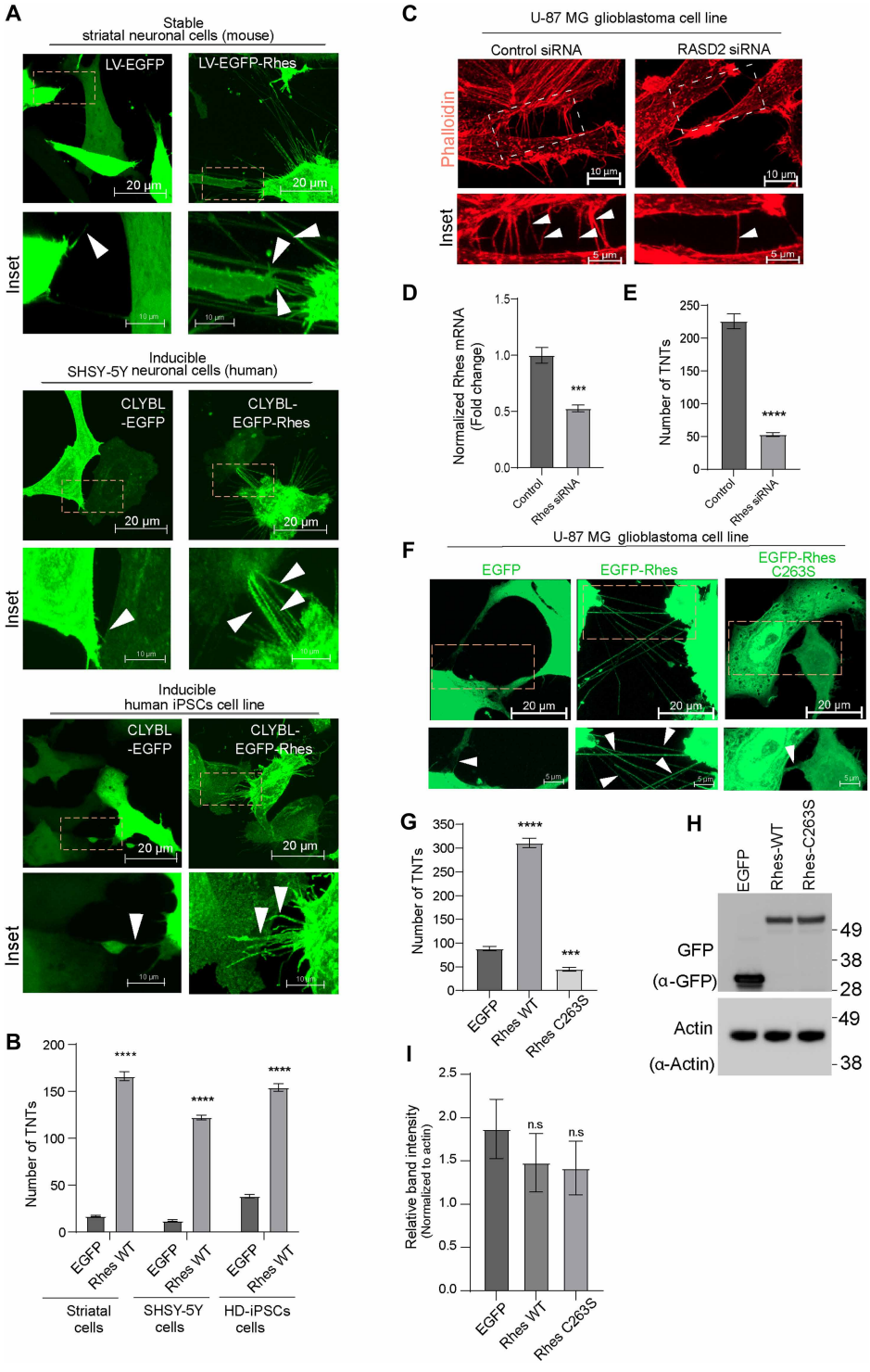

Fig. 1. Membrane-anchored Rhes drives the formation of TNTs between cells. (**A**) Representative confocal images of mouse striatal (STHdh$^{Q7/Q7}$), human SH-SY5Y, and human iPSC–derived cells stably expressing EGFP or EGFP-Rhes (lentiviral) or CLYBL-EGFP or CLYBL-EGFP-Rhes (plasmid), as indicated. Arrowheads denote TNTs connecting adjacent cells. (**B**) Quantification of TNTs from (A), shown as number of TNTs per 100 cells ($n = 3$, independent experiments). (**C**) Confocal images of U-87 MG glioblastoma cells stained with phalloidin following treatment with control or RASD2 siRNA for 72 hours. Arrowheads indicate TNT-like structures. (**D**) Fold change in RASD2 mRNA expression normalized to glyceraldehyde-3-phosphate dehydrogenase (GAPDH), measured by quantitative polymerase chain reaction (qPCR). (**E**) Quantification of TNTs in (C) (TNTs/100 cells, $n = 3$, independent experiments). (**F**) Representative confocal images of U-87 MG glioblastoma cells transfected with EGFP, EGFP-Rhes WT, or EGFP-Rhes C263S plasmids. Arrowheads indicate TNTs. (**G**) Quantification of TNTs from (F) (TNTs/100 cells, $n = 3$). (**H** and **I**) Western blotting analysis of the exogenous expression of EGFP, EGFP-Rhes WT, and EGFP-Rhes C263S detected with GFP antibody and loading control actin (H) and their densitometric quantification (I). Data are presented as means ± SEM. ***$P < 0.001$, ****$P < 0.0001$; Student's t test. n.s, not significant.

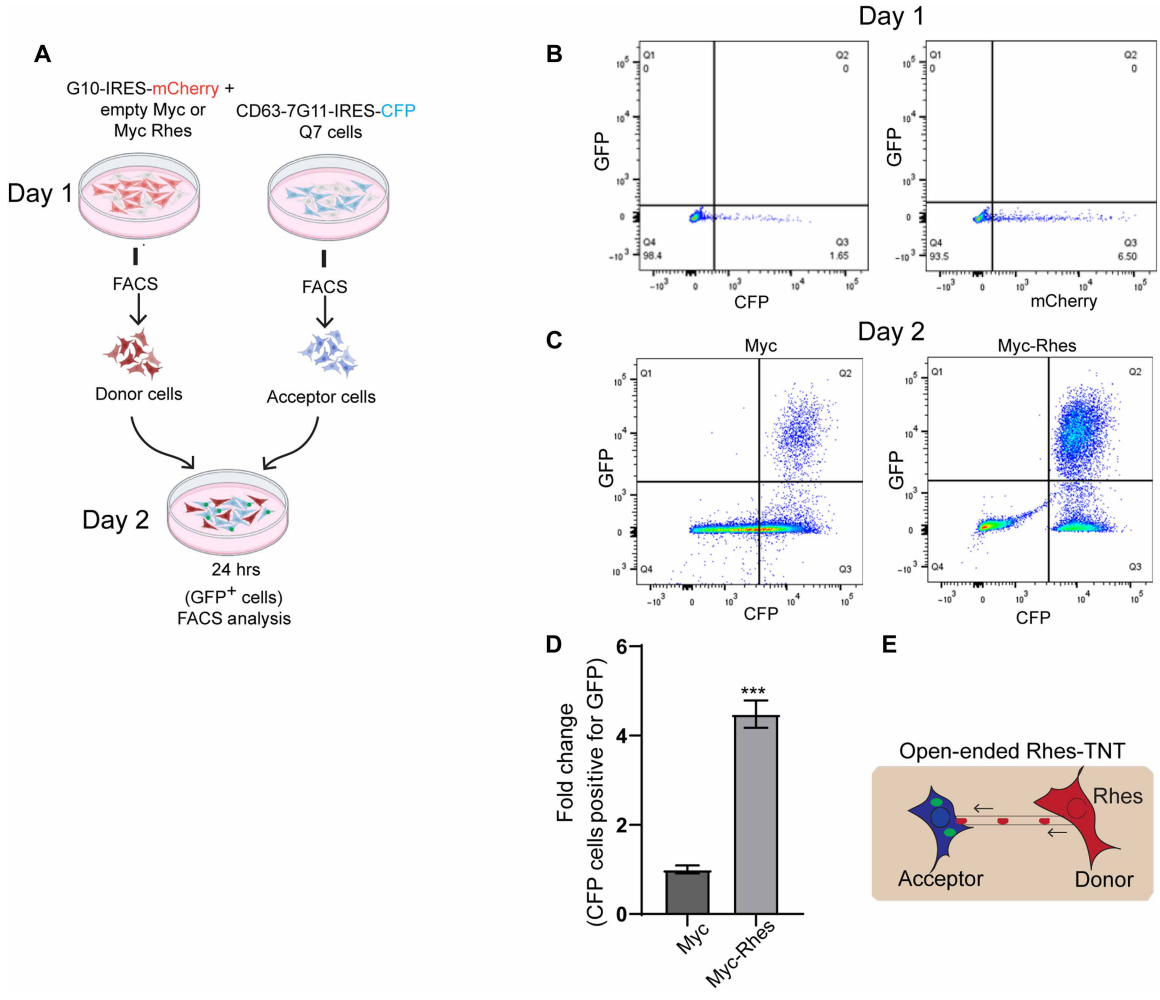

Fig. 2. Rhes promotes open-ended TNTs in striatal neuronal cells. (**A**) Schematic overview of the coculture assay used to assess Rhes-mediated intercellular communication via TNTs. hrs., hours. (**B**) Background GFP plots (day 1) of FACS-sorted striatal neuronal cells expressing CD63-7G11-IRES-CFP and G10-IRES-mCherry. Quadrant 1 (Q1) represents the GFP^+ population, while quadrant 3 (Q3) denotes the CFP^+/$mCherry^+$ cell population. (**C**) FACS-sorted striatal neuronal cells coexpressing CD63-7G11-IRES-CFP with either Myc (control) or Myc-Rhes were cocultured with FACS-sorted striatal cells expressing G10-IRES-mCherry (day 2). After 24 hours, flow cytometry was performed by gating on CFP^+ donor cells to detect GFP signal transfer. Quadrant 2 (Q2) indicates the population of double-positive cells (CFP^+/GFP^+), reflecting direct membrane or cytosolic exchange. (**D**) Quantification of the percentage of CFP^+ cells also positive for GFP. Data are presented as means ± SEM; $^{***}P < 0.001$, Student's *t* test. (**E**) Schematic representation of the proposed model showing how Rhes facilitates open-ended TNT formation to mediate intercellular material exchange.

C to F). In addition, treatment with disodium 4,4′-diisothiocyanato-2,2′-stilbenedisulfonate (DIDS), a pharmacological inhibitor of Slc4a7 (*23*, *24*), also blocked TNT formation (Fig. 4G and H), further validating the role of Slc4a7 in this process. Treatment with Slc4a7 siRNA or DIDS reduced the average TNT length from approximately 30 to 15 μm, without affecting their diameters (fig. S3, A and B). Since DIDS can also block other Slc4a family members, we have used siRNAs approach.

SLC4A7 siRNA, similar to *RASD2* siRNA (Fig. 1, D and E), reduced TNT formation in U-87 cells (Fig. 5, A to C) and shortened TNT length without affecting their diameter (fig. S3, C and D), indicating a role for SLC4A7 in regulating endogenous TNTs. Cotreatment with both *RASD2* and *SLC4A7* siRNAs did not lead to a further reduction in TNT formation (Fig. 5, A to C), suggesting that RASD2 and SLC4A7 function in the same pathway or molecular complex to regulate TNT formation. This likely reinforces the idea that RASD2-SLC4A7 interaction is crucial and rate-limiting in TNT biogenesis. Rhes siRNA and Slc4a7 siRNA both decreased cell viability, suggesting that the Rhes-Slc4a7-TNT pathway may promote the growth of glioblastoma cells (fig. S3E) (*25*). Moreover, DIDS treatment reduced Rhes WT–mediated enhancement of TNT formation but had no effect in cells expressing the membrane-deficient mutant Rhes C263S, indicating that SLC4A7 function is specifically required for membrane-anchored Rhes to promote TNT formation (Fig. 5, D and E).

Rhes colocalizes with Slc4a7 in TNTs

Having established the role of Slc4a7 in Rhes-mediated TNT formation, we next asked whether Rhes and Slc4a7 are physically present within TNTs and, if so, sought to further characterize their interaction. Confocal and stimulated emission depletion (STED) microscopy revealed that Rhes and Slc4a7 are enriched along the length of TNTs (arrow, Fig. 6A) and are in close proximity, as determined by

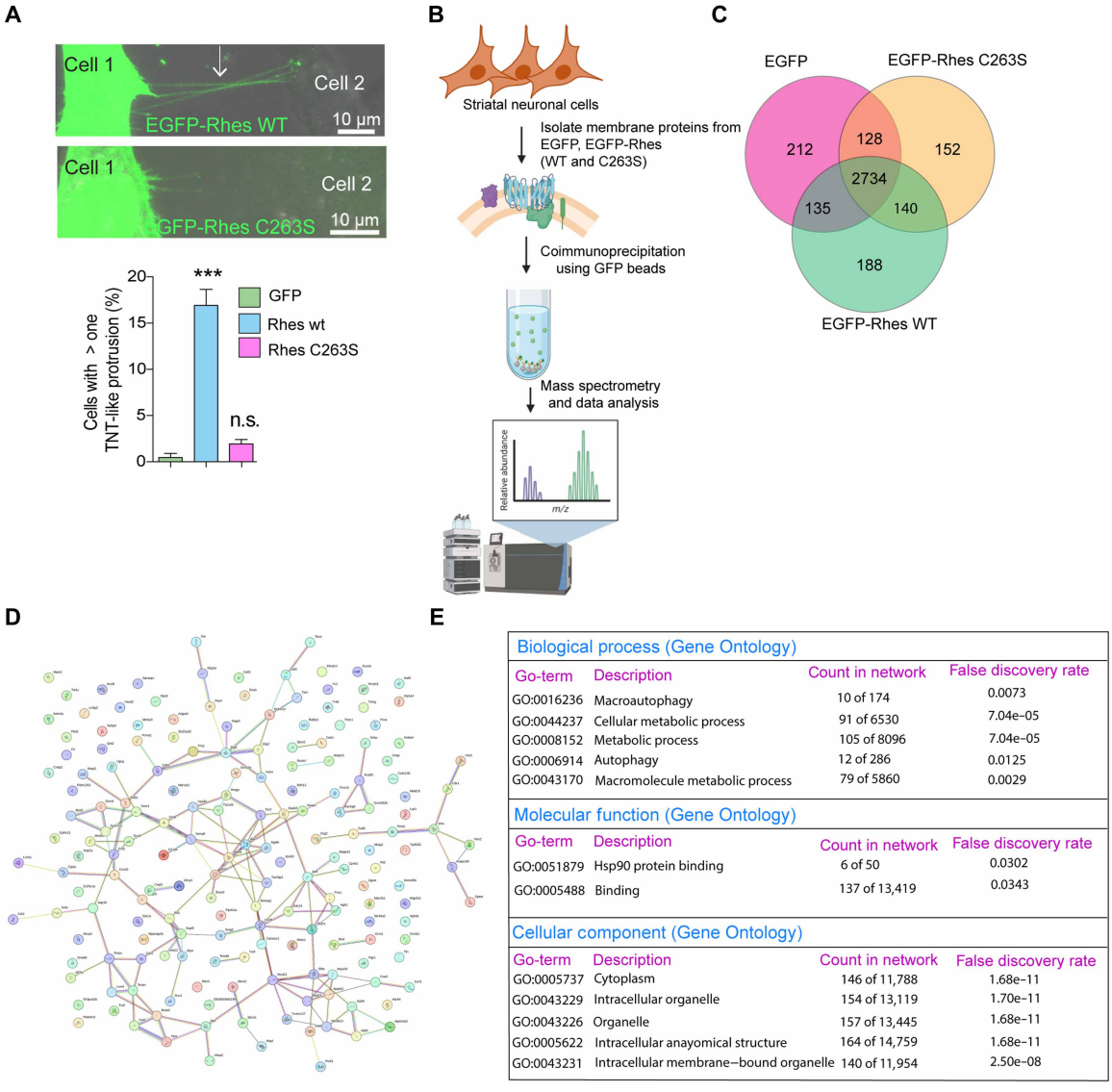

Fig. 3. Membrane-associated protein interactors of Rhes. (**A**) Representative confocal images of striatal neuronal cells expressing either EGFP-Rhes WT or the membrane anchoring–deficient mutant EGFP-Rhes C263S. Arrows indicate TNTs. Quantification of TNTs per 100 cells demonstrates a significant reduction in TNT formation by the C263S mutant. Data are presented as means ± SEM; $P < 0.001$, ***$P < 0.001$; Student's t test. ns, not significant. $n = 210$ to 230 cells per group from three independent experiments. (**B**) Schematic of the experimental workflow used for membrane fractionation and LC-MS/MS analysis to identify Rhes-interacting proteins. (**C**) Venn diagram showing the number of proteins identified with at least two peptides across three conditions: EGFP, EGFP-Rhes WT, and EGFP-Rhes C263S ($n = 3$ per group). (**D**) STRING network analysis of proteins uniquely interacting with EGFP-Rhes WT reveals a subset of membrane-associated proteins . (**E**) Table summarizing the functional enrichment of proteins shown in (D), categorized by biological process, molecular function, and cellular component.

full width at half maximum (FWHM) analysis. FWHM, which measures the width of the fluorescent signal at half its maximum intensity, is a key indicator of spatial resolution and suggested the close apposition of Rhes and Slc4a7 within TNT structures (Fig. 6B). In addition, we observed colocalization of Rhes and Slc4a7 at the base of the TNTs (arrowhead, Fig. 6, A, C, and D).

Biochemical interaction of Rhes with Slc4a7

To gain more insight into their functional relationship, we further characterized the interaction between Rhes and Slc4a7. We confirmed that Rhes-WT, but not the membrane binding–deficient mutant Rhes C263S, copurifies with endogenous Slc4a7 (Fig. 7A). In addition, the guanosine 5′-triphosphate (GTP)–binding–defective mutant Rhes S33N showed similarly reduced interaction with SLC4A7, indicating that both membrane association and GTP binding are important for this interaction. In contrast, mutation of the protein kinase A phosphorylation site at S87 (*26*) had no effect on SLC4A7 binding (Fig. 7B and fig. S4A). Analysis of the cellular localization of these mutants revealed diminished colocalization for S33N and C263S, but not for S87A, compared with the WT Rhes protein (fig. S4, B and C). Thus, Rhes interaction with SLC4A7 depends on its membrane localization and GTP-binding ability, but not on phosphorylation at S87 in Rhes. Note that UniProt and cryo–electron microscopy data indicate that Slc4a7-related proteins are

A

Peptide count

S.No.	Protein name	Protein ID	Exp1	Exp 2	Exp 3	Exp 4
1	Anion exchange protein	SLC4A7	21	7	9	16
2	Plastin-2	LCP1		2	3	3
3	CCR4-NOT transcription complex subunit11	CNOT11		2	2	3
4	Spermatid perinuclear RNA-binding protein	STRBP		2	2	2
5	Regulator of microtubule dynamics protein 3	RMDN3		2		3
6	Twinfilin-2	TWF2		2	2	2
7	WD repeat domain phosphoinositide-interacting protein 2	WIPI2			2	
8	Cluster of Plakophilin-4	PKP4		2		
9	Amyloid-beta A4 precursor protein-binding family B member 2	APBB2			2	2
10	Elongation complex protein 4	ELP4		3	2	2

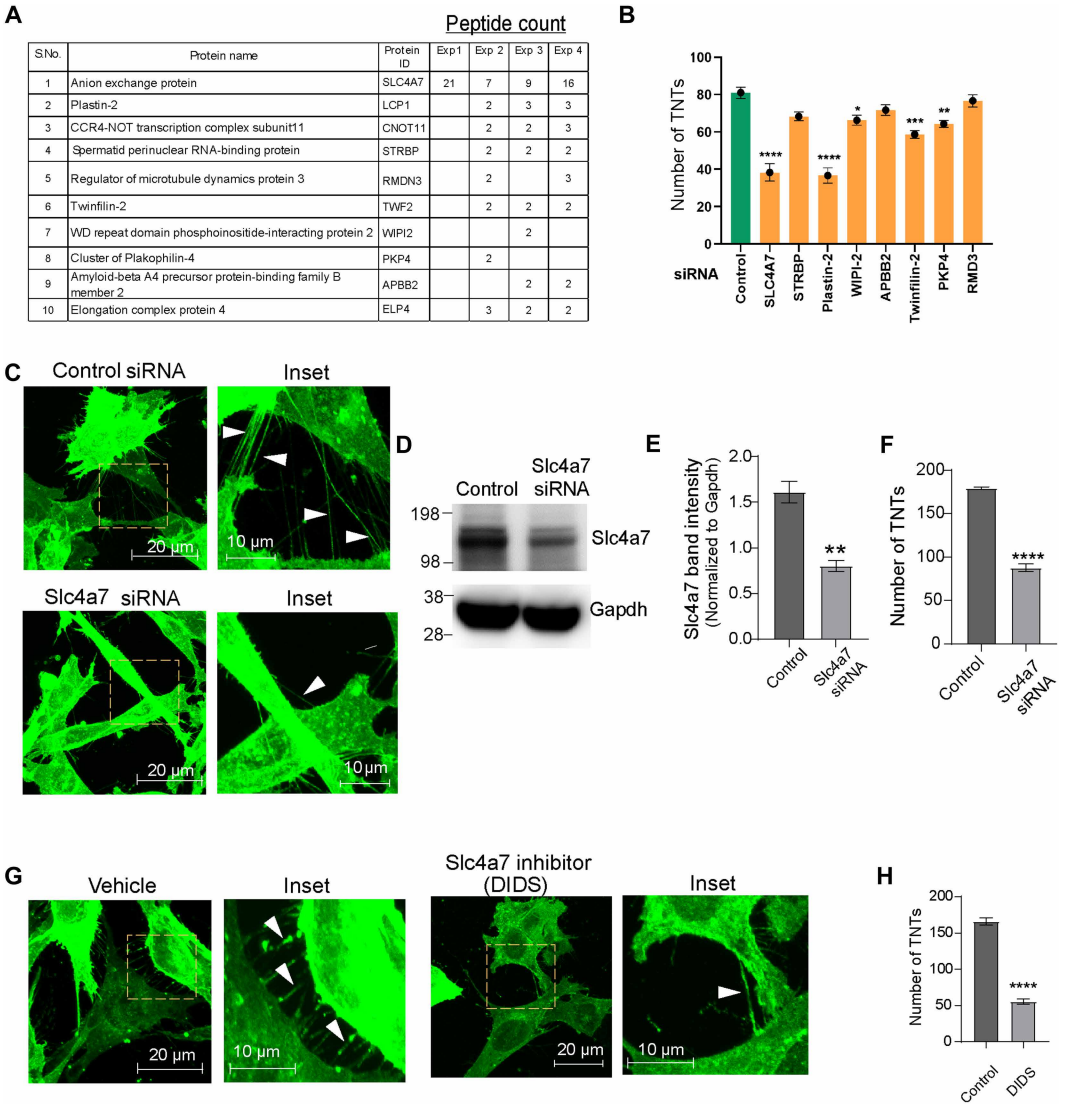

Fig. 4. Slc4a7 mediates Rhes-induced TNT formation. (**A**) Top 10 unique membrane-associated interactors of Rhes identified by LC-MS/MS analysis, ranked by peptide count. (**B**) Quantification of TNTs in striatal neuronal cells following siRNA-mediated knockdown of eight selected interactors from (A), showing the number of TNTs per 50 cells ($n = 3$). (**C**) Representative confocal images of striatal neurons stably expressing EGFP-Rhes following 72-hour transfection with Slc4a7 siRNA. Arrowheads and insets highlight TNTs between neighboring cells. (**D** and **E**) Efficiency of Slc4a7 knockdown was validated by immunoblotting with anti-Slc4a7 and anti-GAPDH antibodies (D), followed by densitometric quantification of Slc4a7 levels (E). (**F**) Quantification of TNTs from (C), reported as TNTs per 100 cells ($n = 3$). (**G**) Representative confocal images of striatal neurons stably expressing EGFP-Rhes treated with vehicle [dimethyl sulfoxide (DMSO)] or the Slc4a7 inhibitor DIDS (100 µM) for 4 to 5 hours. Arrowheads and insets mark TNTs. (**H**) Quantification of TNTs from (G), reported as TNTs per 100 cells ($n = 3$). Data are presented as means ± SEM from three independent experiments; $^{*}P < 0.05$, $^{**}P < 0.01$, $^{***}P < 0.001$, $^{****}P < 0.0001$; Student's *t* test.

glycosylated (*27*) and contain several conserved SUMO and ubiquitin sites, which may account for its mobility shifts.

To further assess whether the interaction between Rhes and Slc4a7 is direct, we copurified hemagglutinin (HA)–SLC4A7 and EGFP-RASD2 from human embryonic kidney (HEK) 293 Expi cells, a high-yield expression system that enables efficient production of recombinant proteins for biochemical analysis. HA nanobeads co-precipitated EGFP-RASD2, and, conversely, EGFP nanobeads pulled down HA-SLC4A7, suggesting a reciprocal and likely direct interaction between the two proteins (Fig. 7C). To further validate this interaction, we independently purified HA-SLC4A7 and EGFP-RASD2 from HEK293 Expi cells. Purified HA-SLC4A7 was incubated with EGFP-nanobody beads bound to either EGFP-RASD2 or used as a nanobody bead control. The results showed that HA-SLC4A7 specifically associated with EGFP-RASD2 but not with the nanobody bead control (Fig. 7D), indicating a direct interaction between the two proteins in vitro.

Last, to confirm the interaction between Rhes and Slc4a7 in living cells, we developed a bioluminescence resonance energy transfer (BRET) assay using NanoLuc (NLuc) fused to SLC4A7 and HaloTag fused to Rhes (Fig. 7E). Upon addition of a fluorescent HaloTag ligand (acceptor), energy transfer occurs from the NLuc donor to the acceptor only if the two proteins are in close proximity, producing a measurable BRET signal. As shown in the time-course plot (Fig. 7F),

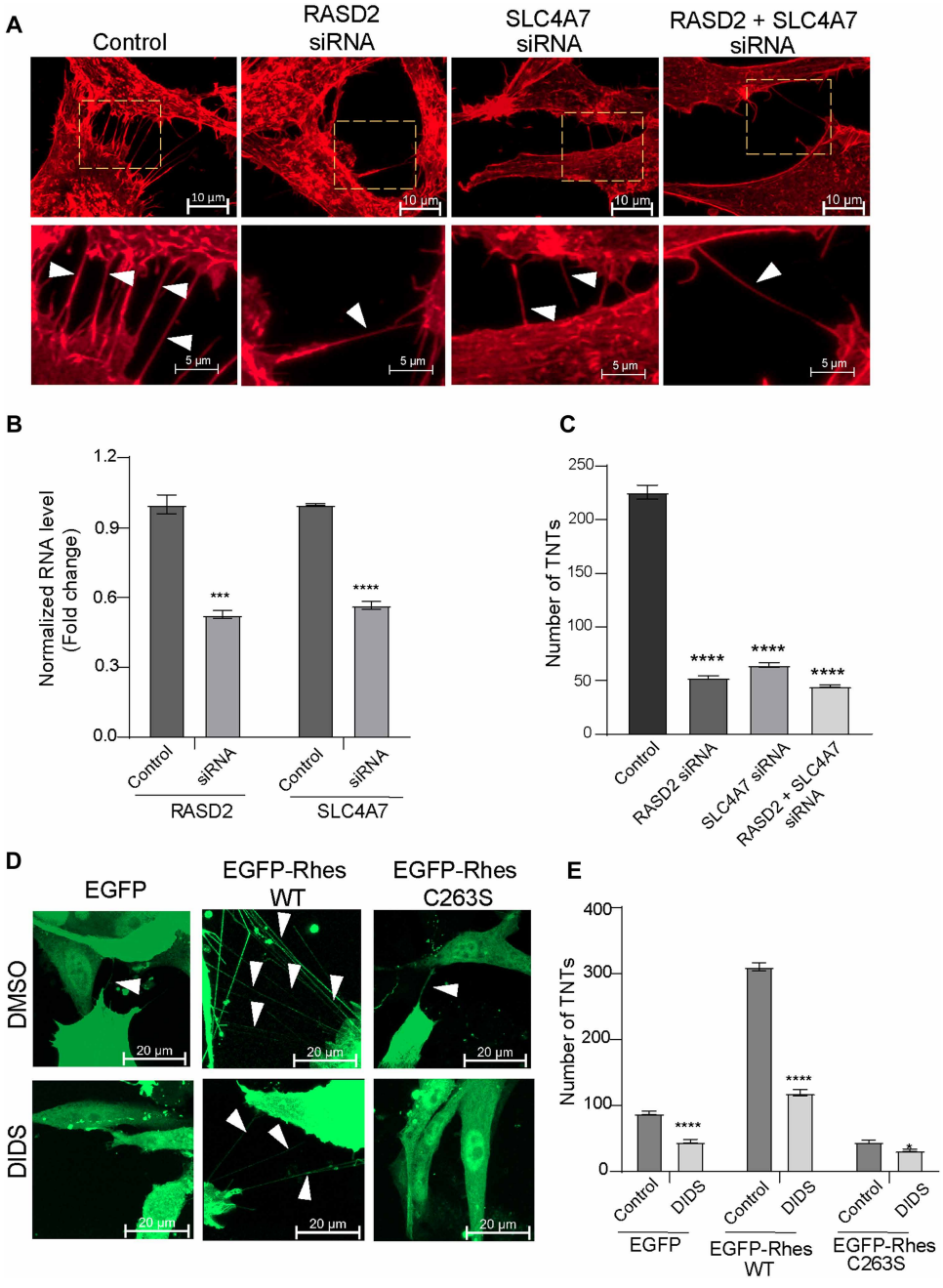

Fig. 5. Rhes and Slc4a7 function in the same molecular complex to regulate TNT formation. (**A**) Confocal images of U87-MG cells treated with siRNA targeting RASD2, SLC4A7, or both. Cells were stained with Phalloidin 72 hours posttransfection to visualize TNTs (arrowheads). (**B**) Fold change in RASD2 and SLC4A7 mRNA expression was assessed by qPCR and normalized to GAPDH. (**C**) Quantification of TNTs from (A) (TNTs/100 cells, $n = 3$). (**D**) Confocal images of U87-MG cells expressing EGFP, EGFP-Rhes, or EGFP-Rhes C263S and treated with either DMSO or DIDS. Arrowheads indicate TNTs between cells. (**E**) TNT quantification from (D) (TNTs/100 cells, $n = 3$). Data are presented as means ± SEM from three independent experiments; ***$P < 0.001$, ****$P < 0.0001$; Student's *t* test.

cells expressing NLuc-SLC4A7 and Halo-Rhes exhibited a stable BRET signal in the presence of the acceptor, while vehicle-treated controls showed minimal signal. Quantification of the BRET ratio (Fig. 7G) revealed a significant increase in energy transfer in the presence of the acceptor, confirming a close physical interaction between Rhes and SLC4A7 in live cells. Because of the lack of a suitable antibody to study this interaction in the brain, we performed coimmunoprecipitation (co-IP) analysis using purified HA-SLC4A7 and mouse striatal lysates. HA-SLC4A7 bound robustly to endogenous Rhes, suggesting that this interaction can occur endogenously in the brain (Fig. 7H). Together, these experiments demonstrate that Rhes closely interacts with SLC4A7 and reinforces the functional relevance of their interaction in the context of Rhes-mediated TNT formation.

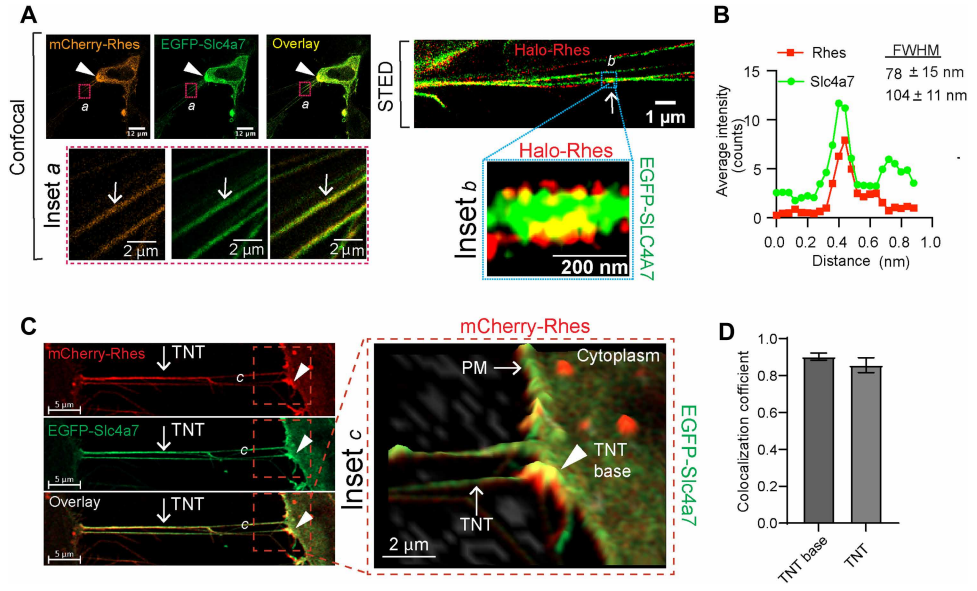

Fig. 6. Rhes colocalizes with Slc4a7 in TNTs and at TNT base. (**A**) Representative confocal (left) and STED (right) images of striatal neuronal cells reveal colocalization of Halo-Rhes (red) and Slc4a7 (green) within TNT-like structures. (**B**) Fluorescence intensity line scan across a TNT-like structure shows the spatial distribution of Rhes and Slc4a7 signals. Rhes exhibits a broader localization (FWHM = 78 ± 15 nm) compared to the more confined signal of Slc4a7 (FWHM = 104 ± 11 nm), indicating differential membrane association. (**C** and **D**) Representative confocal images of striatal neuronal cells showing mCherry-Rhes (red) and Slc4a7 (green) localized along the TNT and at plasma membrane (TNT base) (C), with colocalization quantified by Pearson's coefficient (D). Values represent means ± SEM ($n = 20$).

Rhes binds Slc4a7 via GTP-binding and SUMO E3–like domains and alters membrane pH through Slc4a7

Next, we performed domain mapping to define the regions of Rhes required for interaction with SLC4A7. Glutathione *S*-transferase (GST) pull-down assays using Rhes truncation mutants revealed that both the N-terminal GTP-binding region (residues 1 to 107) and the C-terminal region (residues 171 to 266), which includes the predicted SUMO E3–like domain, contribute to SLC4A7 binding (Fig. 8, A and B). Slc4a7 deletion constructs lacking either the N-terminal or C-terminal region still retained the ability to bind Rhes (Fig. 8C), suggesting that Rhes may associate with internal domains of Slc4a7. These results indicate that Rhes engages Slc4a7 through multiple binding interfaces, with contributions from both its GTP-binding and C-terminal regions (Fig. 8D). This dual-site interaction may underlie a stable and functionally adaptable association between the two proteins. The GTP-binding domain may anchor Rhes to membrane compartments or regulate conformational dynamics, while the SUMO E3–like region may coordinate downstream signaling events or posttranslational modifications, such as SUMOylation. It remains unclear why shorter N-terminal truncations (1 to 71 and 1 to 106) bind SLC4A7, whereas the longer 1 to 216 does not, possibly because of differences in folding, activity, or membrane integration (Fig. 8D). Together, these findings point to a molecular mechanism by which Rhes recruits and regulates Slc4a7 to facilitate TNT formation and intercellular cargo transfer.

Slc4a7 regulates intracellular pH (*16*, *24*). To determine whether Rhes affects membrane-associated pH, we used a ratiometric pH-sensitive reporter construct, Lyn-mCherry-SEpHluorin (Fig. 8F) (*28*–*30*), where mCherry serves as a pH-insensitive control and SEpHluorin responds to pH changes. Cells were transfected with either blue fluorescent protein (BFP) or BFP-Rhes and treated with control or Slc4a7 siRNA (Fig. 8F) (*23*, *24*). Subsequently, a pH calibration curve was generated in U-87 cells expressing Lyn-tagged mCherry-SEpHluorin by exposing the cells to buffers ranging from pH 4.5 to 7.5 (fig. S5, A and B). Live-cell imaging revealed that BFP-Rhes expression increased the SEpHluorin/Lyn-mCherry fluorescence ratio compared with the BFP control, indicating a shift toward a more alkaline membrane–associated pH (Fig. 8, F to I). This effect was significantly reduced upon Slc4a7 depletion (Fig. 8, F to I), suggesting that Rhes alters membrane pH in an Slc4a7-dependent manner. Consistent with this, treatment with the Slc4a7 inhibitor DIDS produced a similar reduction in membrane alkalinization (fig. S5, C and D).

Notably, Lyn-tagged mCherry and SEpHluorin fluorescence signals were markedly enriched at the base of TNTs, indicating localized accumulation at sites of active membrane remodeling during TNT formation (Fig. 8G). This enrichment likely reflects the plasma membrane association of the Lyn-mCherry tag and SEpHluorin. However, immunoblot analysis of membrane-enriched fractions showed no overall change in SEpHluorin protein levels, suggesting that the observed effect is spatial rather than due to altered protein abundance (fig. S5, E and F). These results support a role for Rhes in modulating local pH at the membrane, potentially through its interaction with the bicarbonate transporter Slc4a7.

pH modulation is required for TNT formation but not Rhes-Slc4a7 binding, whereas Rhes farnesylation is essential for both

Next, we investigated whether Rhes binding to Slc4a7 is influenced by Slc4a7 activity. We performed GST pull-down assays in the presence of the anion transport inhibitor DIDS that directly affects pH (Fig. 9A) (*31*). EGFP-Slc4a7 robustly coprecipitated with GST-Rhes across all DIDS concentrations tested, indicating that inhibition of Slc4a7 activity does not disrupt its physical interaction with Rhes (Fig. 9A). However, DIDS treatment markedly reduced both the

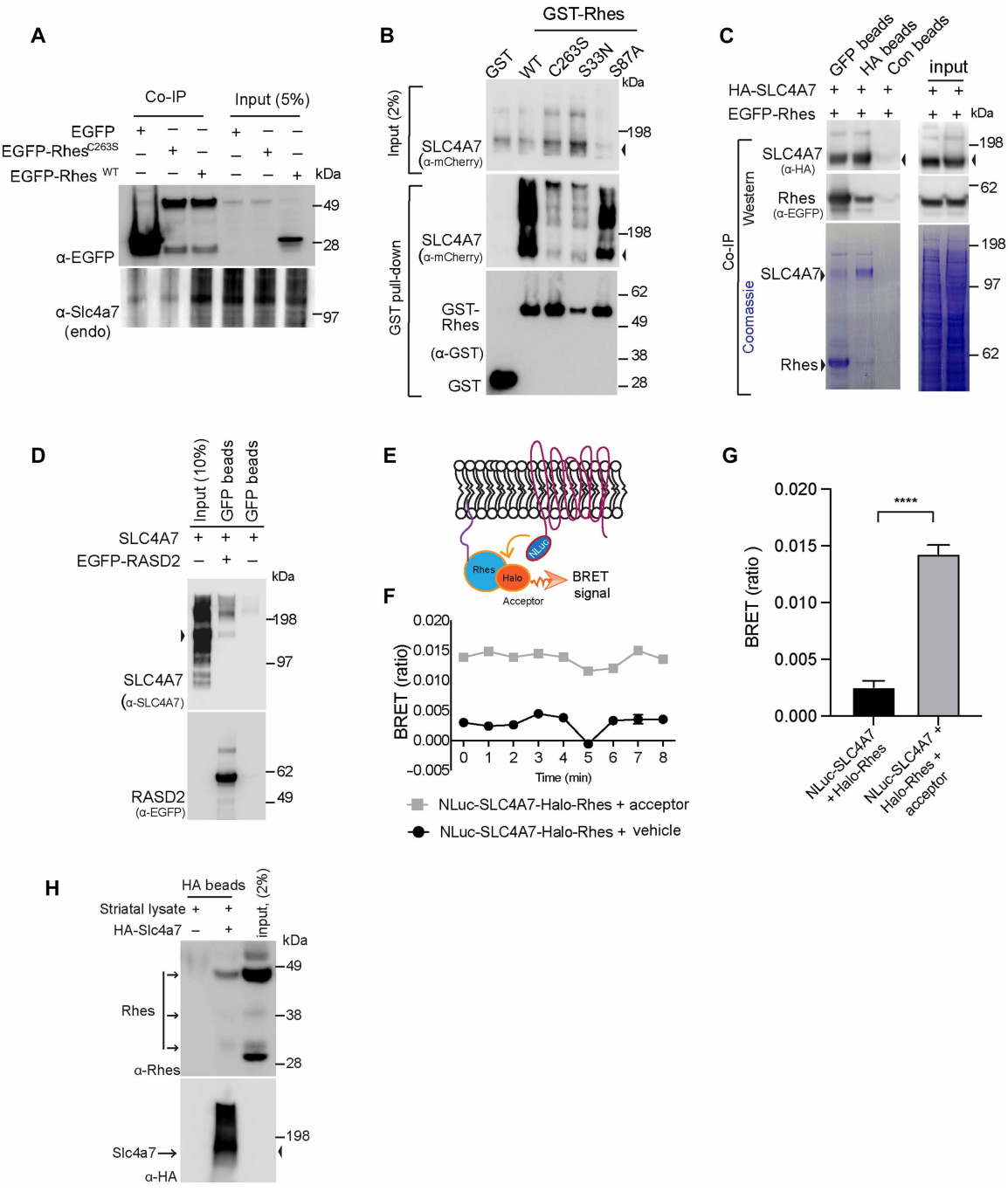

Fig. 7. Rhes directly interacts with Slc4a7 in cultured cells and in mouse brain tissue. (**A**) Immunoprecipitation of EGFP, EGFP-Rhes WT, and EGFP-Rhes C263S from striatal neuronal lysates followed by immunoblotting for endogenous Slc4a7 and GFP reveals reduced Slc4a7 binding with the C263S mutant. (**B**) GST pull-down assay using GST-Rhes WT and mutants (C263S, S33N, and S87A) coexpressed with mCherry-SLC4A7 in striatal cells shows reduced interaction for specific mutants. (**C**) co-IP analysis using HA nanobeads (targeting HA-SLC4A7) and GFP nanobeads (targeting EGFP-RASD2) confirms reciprocal interaction between RASD2 and SLC4A7. (**D**) In vitro–binding assay with purified proteins shows specific interaction of EGFP-RASD2, but not control GFP beads, with SLC4A7. (**E**) Schematic of BRET assay design using NLuc-SLC4A7 and Halo-Rhes constructs in live striatal neuronal cells. (**F**) Time-course plot shows a stable BRET signal in cells coexpressing NLuc-SLC4A7 and Halo-Rhes in the presence of Halo ligand, but not in vehicle controls. (**G**) Quantification of BRET ratios confirms a significant interaction between Rhes and SLC4A7 in living cells. (**H**) Co-IP analysis using HA nanobeads (targeting purified HA-SLC4A7) and striatal mouse brain tissue lysates (targeting Rhes) confirms interaction between Rhes and SLC4A7 in mouse brain. Data represent means ± SEM from three independent experiments; ****$P < 0.0001$, Student's *t* test.

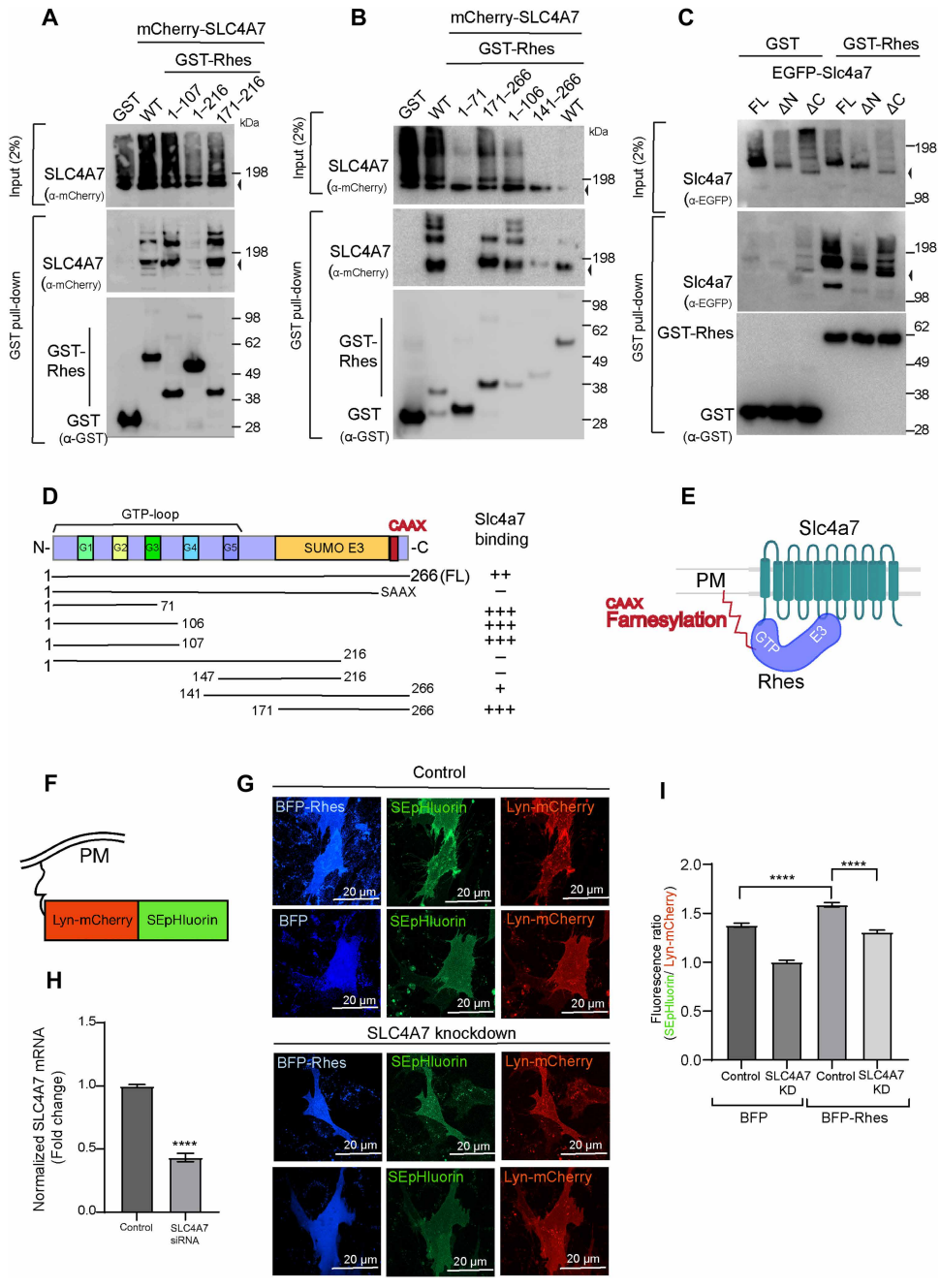

Fig. 8. Rhes binds Slc4a7 via GTP-binding and SUMO E3-like domains and modulates membrane pH via Slc4a7. (**A** and **B**) Mapping of interaction domains using full-length and truncated versions of Rhes, expressed amino acids either as 1-107, 1-216, 171-266 (A) or 1-71, 1-106, 171-266, 141-266 as GST-tagged proteins (B), cotransfected with mCherry-SLC4A7 in striatal neuronal cells. (**C**) GST pull-down assay showing interaction of GST-Rhes WT with EGFP-Slc4a7 FL and deletion constructs lacking either the N terminus (ΔN) or C terminus (ΔC). (**D**) Schematic of Rhes domain architecture, including GTP-binding domains (G1 to G5), a GTP-loop, SUMO E3–like domain, and a C-terminal CAAX box. Binding strength with Slc4a7 is indicated using an arbitrary scale derived from pull-down assays: +++ (strong), ++ (moderate), + (weak), – (none). (**E**) Conceptual model illustrating the two-point interaction between Rhes and Slc4a7, involving both the GTPase and SUMO E3–like domains of Rhes. (**F**) Schematic of the plasma membrane–targeted pH sensor construct, Lyn-mCherry-SEpHluorin, used to detect local pH changes. (**G**) Representative confocal images of U-87 cells coexpressing Lyn-mCherry-SEpHluorin with either BFP or BFP-Rhes in control and Slc4a7 knockdown conditions. (**H**) Fold change in SLC4A7 mRNA expression was assessed by qPCR and normalized to GAPDH. (**I**) Quantification of lyn-SEpHluorin/mCherry fluorescence intensity ratio at the cell periphery reveals Rhes-mediated elevation in membrane-associated pH, which is diminished by Slc4a7 knockdown (KD). Data are presented as means ± SEM from three independent experiments ($n = 30$ cells per condition); ****$P < 0.0001$, Student's t test.

number and length of Rhes-induced TNTs in a dose-dependent manner, without affecting their diameter (Fig. 9, B and C, and fig. S6, A and B), suggesting that Slc4a7 transporter activity or intracellular pH is critical for TNT formation although not for its interaction with Rhes.

In contrast, the farnesyltransferase inhibitor lonafarnib significantly impaired both the interaction between Rhes and Slc4a7 (Fig. 9D) and Rhes-mediated TNT formation, reducing TNT length without affecting their diameter (Fig. 9, E and F, and fig. S6, C and D). Lonafarnib treatment led to dislocation of Rhes, but not Slc4a7, from the membrane, indicating a selective effect on Rhes farnesylation (Fig. 9, G and H, and fig. S7, A to C). We acknowledge however that Lonafarnib can exert its action on TNTs via other small GTPases. As C263S Rhes is inefficient in forming TNTs, our data underscore that membrane-anchored Rhes, through its cysteine farnesylation, is critical for interacting with Slc4a7 and regulating TNT biogenesis.

Slc4a7 inhibition reduces Rhes-mediated cell-to-cell transmission of mHTT

Rhes plays a key role in facilitating cell-to-cell transmission of mHTT via TNTs (*10*). To investigate whether Slc4a7 contributes to this process, we examined its localization and found that Slc4a7, like Rhes, colocalizes with mHTT (N171-82Q) within TNTs (Fig. 10A). Confocal imaging of striatal neuronal cells coexpressing Halo-Rhes, mCherry-mHTT, and GFP-SLC4A7 revealed TNT-like protrusions extending above the substrate plane, connecting neighboring cells (Fig. 10A). Live-cell imaging further demonstrated dynamic transfer of Rhes-, mHTT-, and SLC4A7-positive puncta through these TNTs from one cell to another over time (Fig. 10B and movie S1), indicating active intercellular transport mediated by Rhes-induced TNTs. To directly assess the functional role of Slc4a7 in mHTT transfer, we conducted FACS-based coculture assays (Fig. 10C). Donor Q7 striatal neuronal cells were cotransfected with mCherry-tagged mHTT (N171-89Q) and either EGFP or EGFP-Rhes, while acceptor cells were transfected with BFP alone (Fig. 10C). Following FACS-based purification, donor and acceptor cells were cocultured for 24 hours in the presence of vehicle or the Slc4a7 inhibitor DIDS (Fig. 10C) (*23*, *24*). FACS analysis revealed that BFP^+ acceptor cells cocultured with EGFP-Rhes–expressing donors showed a significant increase in the uptake of both EGFP and mCherry signals (Fig. 10, D and E), indicating transfer of Rhes and mHTT. This transfer was strongly reduced by DIDS treatment. In contrast, minimal transfer was observed in cells expressing EGFP alone, with or without DIDS (Fig. 10, D and E). These findings indicate that Rhes enhances the cell-to-cell transfer of mHTT and that this process requires functional Slc4a7, suggesting a cooperative role for Rhes and Slc4a7 in mediating TNT-based protein transfer.

Slc4a7 regulates mHTT transmission in the brain

Rhes has been shown to promote long-range mHTT propagation in the brain, likely via TNTs (*11*). Since Slc4a7 interacts with Rhes and supports TNT formation in vitro (Fig. 10), we tested whether it also contributes to mHTT spread in vivo. To assess this, we injected a dual-reporter lentiviral construct encoding EGFP and mCherry-tagged mHTT separated by a P2A sequence (Fig. 11A) into the striatum of WT and global Slc4a7 knockout (KO) mice (Fig. 11B). After 12 weeks, the brain sections were analyzed for the distribution of EGFP and mHTT (mCherry) signals. Confocal imaging revealed robust mHTT spread from the injection site in WT mice, with mCherry signal observed up to 1000 μm away (Fig. 11, C and D). In contrast, Slc4a7-KO mice exhibited a marked reduction in mHTT distribution beyond the injection site, while EGFP expression remained largely restricted to the site of injection in both genotypes. Quantification (Fig. 11D) confirmed significantly lower mHTT signal intensity at 250, 500, and 1000 μm away from the injection site in Slc4a7-KO mice compared to WT, whereas EGFP and 4′,6-diamidino-2-phenylindole (DAPI) (nuclei) signal intensities showed no significant differences across conditions. Moreover, the protein levels of mHTT remained unchanged between control and Slc4a7 knockdown conditions (fig. S8, A to C), suggesting that Slc4a7 is unlikely to alter or promote degradation of mHTT protein. Collectively, these findings indicate that Slc4a7 is required for the long-range propagation of mHTT in the brain, without affecting local transgene expression or cell density.

DISCUSSION

We identify Slc4a7 as a previously unidentified mediator of cell-to-cell communication, acting in concert with Rhes to promote TNT formation and cargo transmission. Our data show that Rhes directly interacts with Slc4a7 and modulates its activity, facilitating TNT-based intercellular transport, including mHTT (Fig. 11E). This model proposes that the interaction between Rhes and Slc4a7 facilitates the formation of TNTs by coordinating membrane signaling and cytoskeletal dynamics. Slc4a7, a sodium-coupled bicarbonate transporter, brings Na^+ and HCO_3^- into the cell, contributing to localized pH modulation. Rhes, a membrane-anchored small GTPase, binds to Slc4a7 through both its N- and C-terminal domains. While this interaction is independent of Slc4a7's transport activity, it occurs at membrane sites where Slc4a7 is active. From LC-MS/MS analysis, Rhes is found to associate with Plastin, a known actin-bundling protein. This suggests that Rhes may promote actin remodeling at the membrane, supporting TNT formation. The model speculates that elevated pH, presumably due to bicarbonate influx, could create a favorable environment for actin polymerization (*32*–*34*) and bundling, further aiding TNT biogenesis. However, detecting TNTs in the brain remains technically challenging because of the limited availability of high-resolution imaging of TNT nanostructures, the absence of definitive molecular markers, and the extreme fragility of TNTs under conventional fixation conditions. Although some mechanistic steps remain hypothetical, the model highlights a potential Rhes-Slc4a7-Plastin axis that links membrane-associated signaling to TNT formation (Fig. 11E).

Slc4a7 is widely expressed in peripheral tissues and the brain, with highest levels observed in the cortex and hippocampus (*35*, *36*). Although Rhes is enriched in the striatum, it is also present in cortical and hippocampal regions (*37*), suggesting that Rhes-Slc4a7 interaction may influence communication beyond the striatum. Slc4a7 plays a critical role in cellular proton (H^+) regulation. Its loss leads to hearing loss and occasional visual impairment (*14*, *38*, *39*), mimicking features of Usher syndrome—a genetic disorder affecting hearing and vision. However, no SLC4A7 mutations have been identified in patients with Usher, suggesting that while Slc4a7 dysfunction phenocopies the disease, it is not a direct genetic cause (*40*).

Rhes and Slc4a7 share overlapping functions in the brain. Genetic variation in SLC4A7 is associated with susceptibility to addiction in humans (*41*). In animal models, Slc4a7 deletion increases

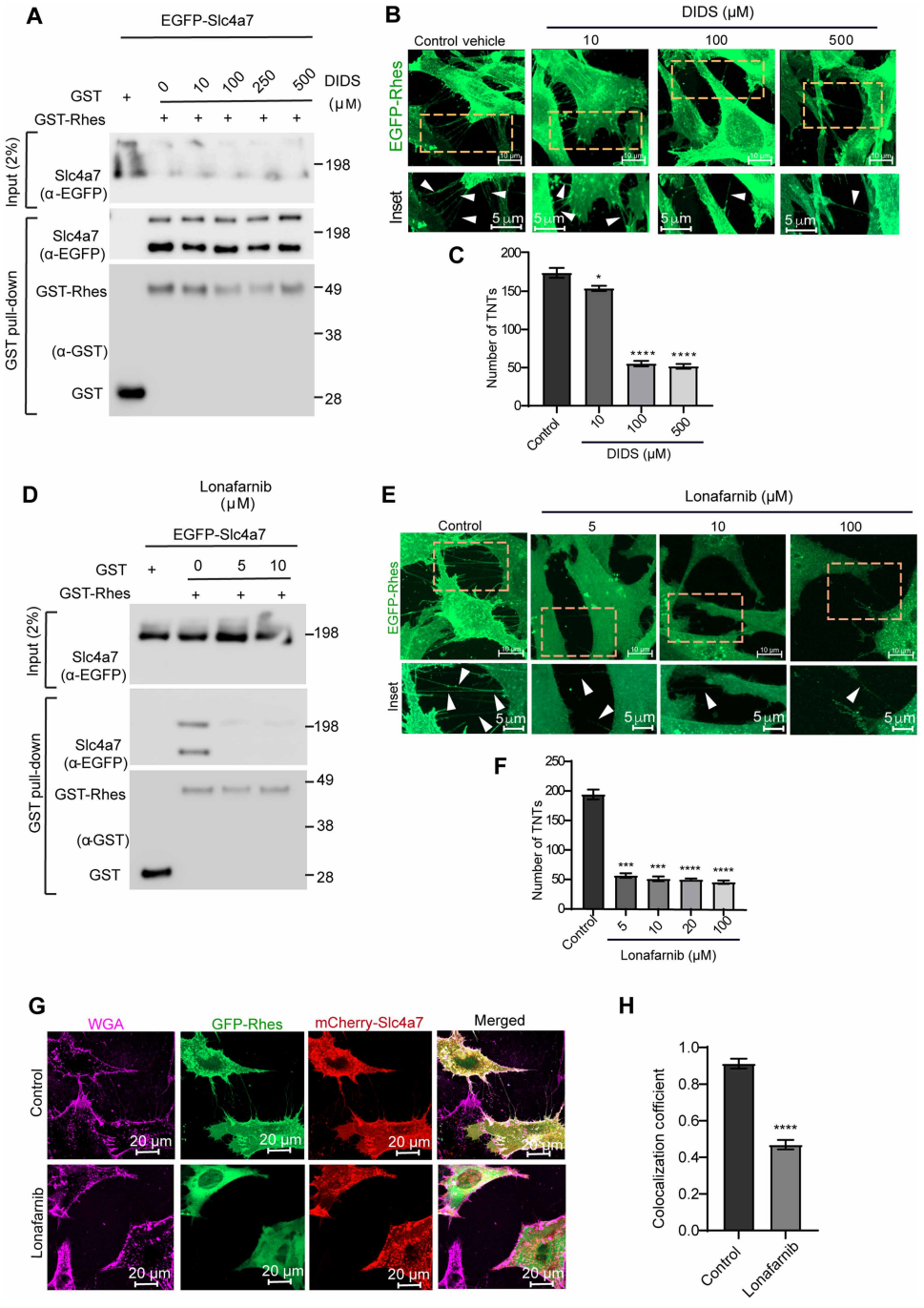

Fig. 9. pH modulation is required for TNT formation but not Rhes–Slc4a7 binding, whereas Rhes farnesylation is essential for both. (**A**) Representative immunoblots of GST pull-down assays from striatal neuronal cells coexpressing GST-Rhes and EGFP-Slc4a7, treated with increasing concentrations of the Slc4a7 inhibitor DIDS. Binding of Rhes to Slc4a7 remains unaffected by DIDS. (**B**) Representative confocal images of striatal neuronal cells stably expressing EGFP-Rhes treated for 4 hours with the indicated concentrations of DIDS. Insets and arrowheads highlight TNTs connecting adjacent cells. (**C**) Quantification of TNTs per 100 cells from (B), showing a dose-dependent reduction in TNT formation ($n = 3$). (**D**) GST pull-down assay showing that increasing concentrations of the farnesyltransferase inhibitor lonafarnib impair the interaction between GST-Rhes and EGFP-Slc4a7 in striatal neuronal cells. (**E**) Representative confocal images of striatal neuronal cells stably expressing EGFP-Rhes following lonafarnib treatment. Insets and arrowheads indicate TNT structures. (**F**) Quantification of TNTs from (E), showing significant inhibition of TNT formation by lonafarnib in a dose-dependent manner (TNTs per 100 cells; $n = 3$). (**G**) Representative confocal images of striatal neuronal cells coexpressing EGFP-Rhes and mCherry-Slc4a7 following lonafarnib treatment. Plasma membrane labeled with wheat germ agglutinin (WGA). (**H**) Quantification of colocalization between Rhes (green) and Slc4a7 (red) at cell periphery from (G) using Pearson's coefficient ($n = 20$). Data represent means ± SEM from three independent experiments; $^{*}P < 0.05$, $^{***}P < 0.001$, $^{****}P < 0.0001$; Student's *t* test.

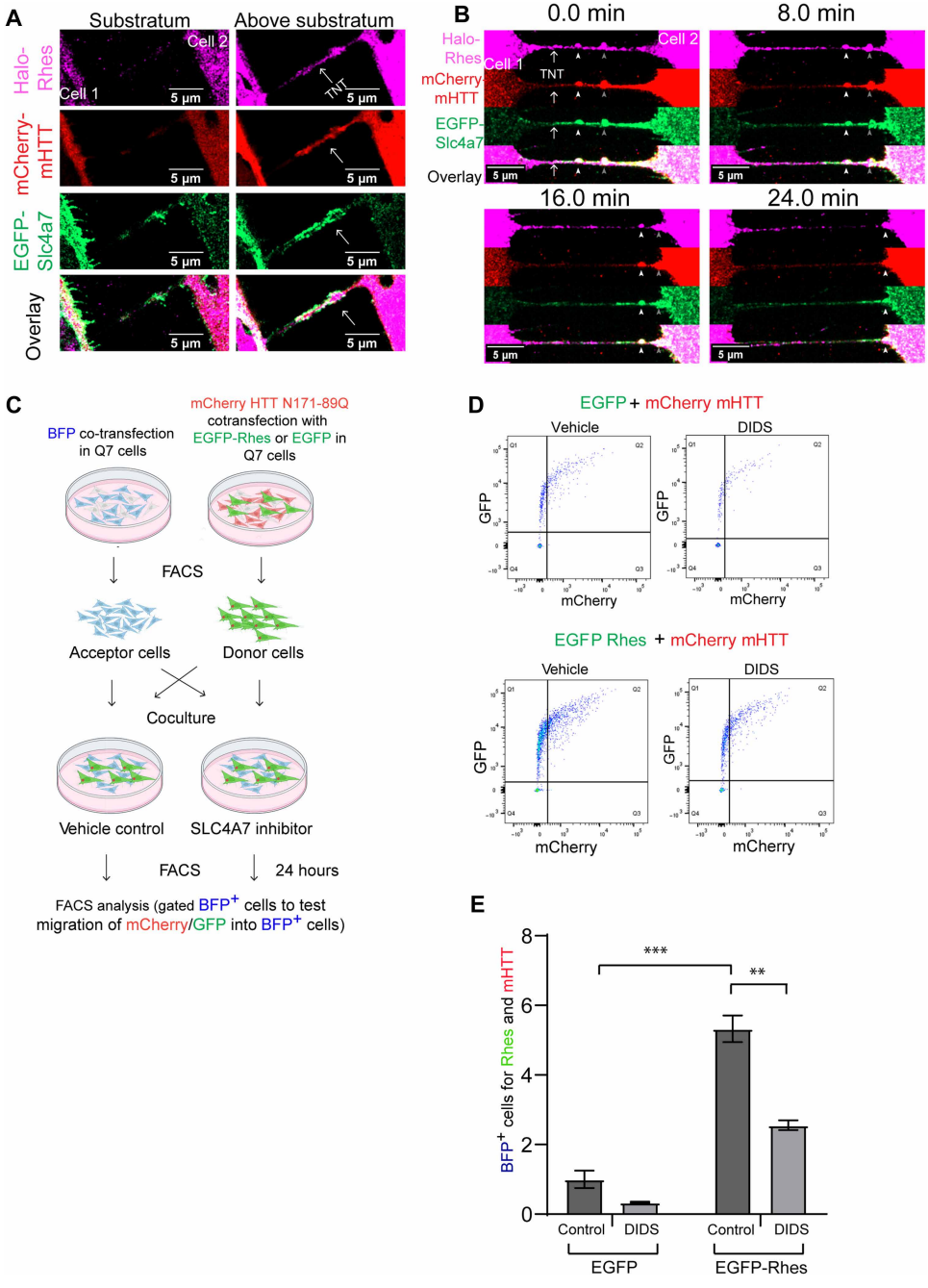

Fig. 10. Slc4a7 inhibition reduces Rhes-mediated cell-to-cell transmission of mHTT. (**A**) Confocal image of striatal neuronal cell expressing Halo-Rhes, mCherry-mHTT (171-82Q), and GFP-Slc4a7 shows two different planes (substrate plane or above substrate). Arrow points to TNT-like cellular protrusion visible above the substrate plane from cell 1 to cell 2. (**B**) Live-cell imaging of striatal neuronal cells expressing Halo-Rhes, mCherry-HTT, and GFP-Slc4a7. Arrowheads (white) indicate Rhes-mHTT-Slc4a7–positive puncta delivery from cell 1 to cell 2 at indicated time stamps.). See related movie S1. (**C**) Schematic of the coculture experimental setup used for assessing intercellular transfer of mHTT in the presence or absence of Rhes and Slc4a7 activity with DIDS (100 µM). (**D**) FACS plot showing the gating strategy for BFP-positive striatal neuronal cells following coculture with cells transfected with mHTT and Rhes constructs as indicated. A total of 5000 BFP-positive cells were recorded for each condition. (**E**) Quantification of the percentage of BFP-positive cells that also exhibit GFP and mCherry fluorescence, indicating successful transfer of mHTT. Data represent means ± SEM from three independent experiments; $^{**}P < 0.01$, $^{***}P < 0.001$; one-way analysis of variance (ANOVA).

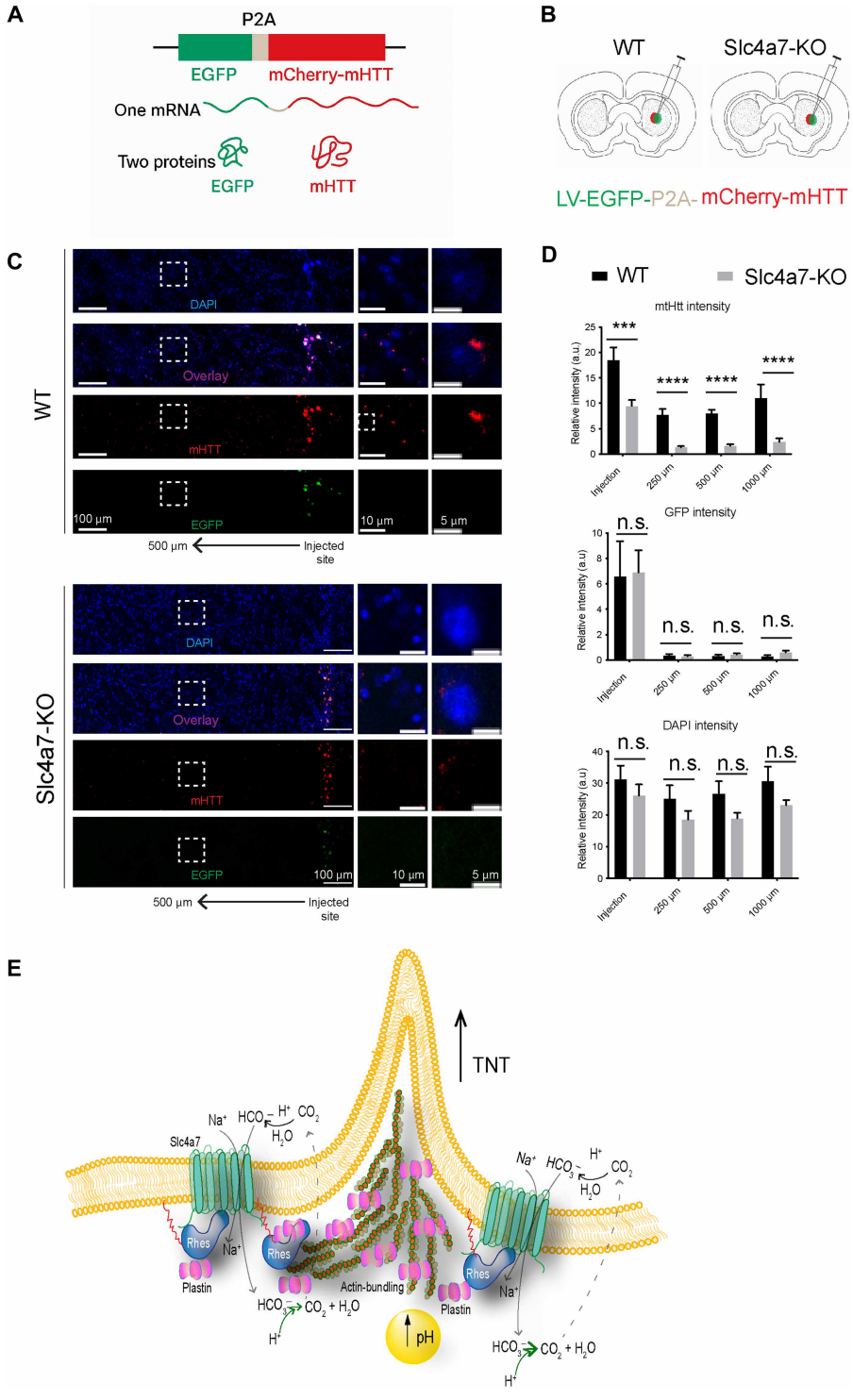

Fig. 11. Slc4a7 regulates mHTT spread in the brain. (**A**) Schematic of lentiviral (LV) vector constructs used for in vivo delivery of EGFP and mHTT. (**B**) Experimental design depicting stereotaxic injection of LV into the striatum of WT and Slc4a7 KO mice. (**C**) Representative confocal images of brain sections showing EGFP (green) and mHTT (red) fluorescence at the injection site and at 500-µm distance. Insets highlight perinuclear mHTT localization (arrowheads), and nuclei are stained with DAPI (blue). (**D**) Quantification of relative fluorescence intensity of mHTT (top), EGFP (middle), and DAPI (bottom) at distances of 250, 500, and 1000 µm from the injection site. mHTT signal spread is significantly attenuated in Slc4a7 KO mice. (**E**) Model showing that Rhes-Slc4a7 interaction promotes TNT formation via pH modulation and actin remodeling. Data represent means ± SEM; ****$P < 0.0001$, n.s., not significant; two-way ANOVA with Bonferroni post hoc test. a.u., arbitrary units.

alcohol intake and affects anxiety-like locomotor behavior (*14*, *42*). Similarly, Rhes deletion enhances cocaine-induced motor stimulation and alters anxiety-like responses (*43*, *44*). Both proteins also modulate glutamate toxicity: Slc4a7 deletion protects against *N*-methyl-D-aspartate (NMDA)–induced excitotoxicity (*45*, *46*), and Rhes promotes NMDA receptor–mediated toxicity, which is mitigated in Rhes KO models of Huntington disease (HD) (*47*–*49*).

Beyond neurological roles, both proteins are implicated in cancer. Slc4a7 is up-regulated in primary breast tumors and metastases (*50*, *51*), and its deletion suppresses breast cancer development (*52*, *53*). Rhes is elevated in uveal melanoma and thyroid cancer (*54*); its depletion reduces tumor growth and metastasis (*54*, *55*). Rhes and SLC4A7 also converge on mammalian target of rapamycin Complex 1 (mTORC1) signaling. Rhes activates mTORC1 in striatal neurons, contributing to L-DOPA–induced dyskinesia (*56*), while mTORC1 stimulates SLC4A7 translation in dividing cells to increase bicarbonate uptake for nucleotide synthesis (*57*). Together, these pathways show how Rhes and SLC4A7 link through mTORC1 to regulate cell growth and neurological function in both cancer and brain disorders.

A growing body of evidence supports a role for TNTs in cancer progression (*58*–*62*). TNTs mediate transfer of GTPases (e.g., Rab5, Rab11, and Kras), chemotherapeutic agents (e.g., daunorubicin), and cellular organelles including mitochondria (*60*, *63*–*68*). They also facilitate communication between tumor cells and macrophages, contributing to metastasis (*69*). TNT-mediated transfer of microRNAs such as miR-155 has been shown to drive bladder cancer progression (*70*). Our findings that Rhes and Slc4a7 promote TNT formation suggest a broader role for these proteins in the pathological spread of misfolded proteins in both neurodegenerative diseases and cancer. While Rhes and Slc4a7 likely mediate the transfer of various cellular cargos, our study specifically demonstrates their role in the intercellular transmission of mHTT within the striatum. Cell-to-cell propagation of mHTT is well-established in HD models and patient tissues (*2*). Although Slc4a7 has not been widely linked to neurodegeneration, it is up-regulated in Frontotemporal lobar degeneration (FTLD)-tau (*71*) and functions as a key Na^+/HCO_3^- cotransporter in the intestinal epithelium (*72*), an emerging site of gut-brain communication that may influence protein aggregation and spread (*73*). In addition, Rhes has been implicated in promoting tau toxicity, and its abnormal localization is a hallmark of tauopathies (*74*, *75*). Together, the involvement of Rhes in both mHTT and tau pathologies, along with its interaction with Slc4a7, suggests a shared mechanism facilitating protein spread and neurotoxicity across multiple neurodegenerative diseases. Therefore, targeting the Rhes-Slc4a7 axis could represent a therapeutic strategy to disrupt TNT-mediated intercellular communication and limit the dissemination of pathogenic proteins in neurodegeneration and cancer.

MATERIALS AND METHODS

Cell culture

Mouse STHdhQ7/Q7 striatal neuronal cells (Q7) were cultured at 33°C in Dulbecco's modified Eagle's medium (DMEM; Thermo Fisher Scientific) supplemented with 10% fetal bovine serum (FBS), following previously published protocols (*10*). SH-SY5Y neuroblastoma and U-87 MG glioblastoma cells were also maintained in DMEM with 10% FBS. These cells were cultured at 37°C in a humidified incubator with 5% CO_2 and passaged every 2 to 3 days when ~80% confluent. Experiments were performed between passages 5 and 20.

Expi293 cells, a suspension-adapted HEK293 derivative, were grown in Expi293 expression medium (Thermo Fisher Scientific, catalog no. A1435101) under manufacturer-recommended conditions. Cultures were maintained in sterile vented Erlenmeyer flasks (Corning) at 37°C with 8% CO_2 and shaken at 125 rpm.

The HD-iPSCs used in our study are reprogrammed from fibroblasts of a patient with HD carrying an expanded CAG repeat length of 72. This HD-specific iPSC (HD-iPSC) line was originally generated by Park *et al.* (*76*). Patient-derived HD iPSCs were cultured on Matrigel-coated (1:100 in cold DMEM/F12) plates in mTeSR1 medium (STEMCELL Technologies, catalog no. 85850). After adding Matrigel, the plates are incubated at 37°C, before adding cells. iPSCs were passaged every 4 to 6 days using 0.5 mM EDTA (Promega, V4231) in phosphate-buffered saline (PBS) and maintained between 30 and 70% confluency to avoid spontaneous differentiation. All cultures were maintained at 37°C in 5% CO_2.

Generation of stable cell lines

Stable cell lines expressing EGFP or EGFP-Rhes WT were generated in STHdhQ7/Q7, SH-SY5Y, and HD-iPSCs. For Q7 striatal neuronal cells, lentiviral constructs encoding EGFP or EGFP-Rhes WT were obtained from VectorBuilder. Cells were infected with viral particles, and, 48 hours postinfection, EGFP-positive cells were sorted by FACS and expanded for downstream experiments.

For SH-SY5Y and HD-iPSCs, stable expression was achieved using CLYBL-targeted constructs encoding EGFP or EGFP-Rhes WT. These constructs also included a constitutively expressed mApple reporter to facilitate selection. Cells were transfected with CLYBL-EGFP or CLYBL-EGFP-Rhes WT, and 48 hours posttransfection, mApple-positive cells were sorted by FACS and expanded. To induce EGFP expression from the CLYBL locus, cells were treated with doxycycline (1 μg/ml; Sigma-Aldrich, D9891). EGFP fluorescence became visible approximately 24 hours postinduction, at which point cells were used for imaging.

Plasmid constructs

The coding sequences of EGFP and EGFP-Rhes WT were subcloned into the CLYBL-TO-hNGN2-BSD-mApple vector (Addgene plasmid #124229) between the BamHI and NruI restriction sites. Rat GFP-Slc4a7-FL was gifted to us by S. F. Pedersen (University of Copenhagen). Delta N (Δ1 to 148) and Delta-C (Δ 1118 to 1254) terminal constructs of Slc4a7 were cloned in pEGFP-C1 vector using the restriction enzymes BglII and KpnI. Positive clones were confirmed by Sanger sequencing. Rat Rhes-WT and its deletion mutants (indicated in the Fig. 8) were subcloned from their respective Myc-tagged constructs into the plasmid Cytomegalovirus (pCMV)-GST vector backbone using SalI and NotI restriction enzymes. The full-length human Rhes was inserted into a mammalian expression vector (pCMV) containing an N-terminal (His)10 -tag followed by a GFP as an expression marker and a precision protease cleavage site VectorBuilder.

The full-length human *SLC4A7* was inserted into a mammalian expression vector (pCMV) containing an N-terminal HA tag followed by an mCherry as an expression marker and a precision protease site (VectorBuilder). The full-length human *RASD2* was inserted into a mammalian expression vector (pCMV) containing an N-terminal EGFP tag an expression marker and a precision protease site (VectorBuilder).

Below is the list of primers used in the study.
CLYBL-EGFP-FP GCGGATCCATGGTGAGCAAGGGCGAGG
CLYBL-EGFP-RP GATCGCGACTTGTACAGCTCGTCCATGCC
Delta-N-Slc4a7-FP GCAGATCTAGATCCGCTAGCATGGATG-GTGG
Delta-N-Slc4a7-RP GAGGTACCCATGCTAGCGGATCTGAC
Delta-C-Slc4a7-FP GCAGATCTATGGAGGCAGACGGGGCCGG
Delta-C-Slc4a7-RP CCGGTACCAGCATCCATGTATTTTTTTG-ATGGTT
Human SLC4A7-FP [quantitative polymerase chain reaction (qPCR)]CCAGTCGGATTCCTCTTGTTCG
Human SLC4A7-RP (qPCR)CAGACCTGTTCGCAAAGAGTGG
Human RASD2-FP (qPCR) GGGAGCCACCACAGACTC
Human RASD2-RP (qPCR) CTGGACAAAGTCTTCATCATGG
Human [glyceraldehyde-3-phosphate dehydrogenase (GAPDH)–FP (qPCR) AGCCACATCGCTCAGACAC
Human GAPDH-RP (qPCR) GCCCAATACGACCAAATCC

Membrane fraction isolation

To identify membrane-bound interactors of Rhes, MS was performed on EGFP, EGFP-Rhes WT, and the membrane binding–deficient mutant EGFP-Rhes C263S. Each condition was processed in biological triplicates.

Q7 striatal cells were seeded in 10-cm dishes and transfected with 8 μg of plasmid DNA using Lipofectamine 2000 (Thermo Fisher Scientific, catalog no. 11668027). Two 10-cm dishes were used per construct. At 48 hours posttransfection, membrane protein fractions were isolated using the Mem-PER Plus Membrane Protein Extraction Kit (Thermo Fisher Scientific, catalog no. 89842), following the manufacturer's protocol.

Membrane fractions were then incubated overnight at 4°C with ChromoTek GFP-Trap Agarose beads (catalog no. gta) to immunoprecipitate GFP-tagged proteins and their interactors. The next day, the beads were washed five times with the wash buffer to remove nonspecific binders. Bound proteins were eluted in 2× LDS sample buffer (Invitrogen) supplemented with 5% β-mercaptoethanol (β-ME), followed by heating at 95°C for 10 min. The final eluates were submitted to the institutional proteomics core facility for LC-MS/MS analysis.

Mass spectrometry

Protein solutions in Laemmli sample buffer were heated at 95°C for 10 min and then electrophoresed into a 4 to 20% Mini-PROTEAN TGX precast protein gels from Bio-Rad (Hercules, CA) for 10 min using 120 V. The gels were then stained with Coomassie for 1 hour and destained in water overnight. The gel section containing stacked proteins was cut out, and proteins were in-gel digested with trypsin (Pierce Biotechnology, Rockford, IL) for 1 hour at 50°C using ProteaseMax Surfactant trypsin enhancer following reduction and alkylation with dithiothreitol and iodoacetamide, respectively, according to the manufacturer's instructions (Promega Corporation, Madison, WI). LC-MS/MS analysis of extracted peptides was subsequently carried out using an Orbitrap Fusion Tribrid mass spectrometer, following 2-mg capacity ZipTip (Millipore, Billerica, MA) C18 sample clean-up according to the manufacturer's instructions. Peptides were eluted from an EASY PepMapTM RSLC C18 column (2 mm, 100 Å, 75 mm by 50 cm, Thermo Fisher Scientific, San Jose, CA) into the mass spectrometer using a gradient of 5 to 25% solvent B (80/20 acetonitrile/water, 0.1% formic acid) in 90 min, followed by 25 to 44% solvent B in 30 min, 44 to 80% solvent B in 0.10 min, a 10-min hold of 80% solvent B, a return to 5% solvent B in 3 min, and finally with another 3-min hold of 5% solvent B. The gradient was then extended for the purpose of cleaning the column by increasing solvent B to 98% in 3 min, a 98% solvent B hold for 10 min, a return to 5% solvent B in 3 min, a 5% solvent B fold for 3 min, an increase of solvent B to 98% in 3 min, a 98% solvent B hold for 10 min, a return to 5% solvent B in 3 min, a 5% solvent B hold for 3 min, and finally, another increase to 98% solvent B in 3 min followed a hold of 98% solvent B for 10 min. All flow rates were 250 nl/min, delivered using an nEasy-LC1000 nano LC system (Thermo Fisher Scientific, San Jose, CA). Solvent A consisted of 0.1% formic acid. Ions were created with an EASY Spray source (Thermo Fisher Scientific, San Jose, CA) held at 45°C using a voltage of 1.7 or 2.5 kV. Data-dependent scanning was performed by the Xcalibur v 4.7.69.37 software using a survey scan at 120,000 resolution in the Orbitrap analyzer scanning mass/charge ratio 380 to 2000 followed by higher-energy collisional dissociation MS/MS at a normalized collision energy of 30% of the most intense ions at maximum speed at an automatic gain control of 1.0×10^4. Precursor ions were selected by the monoisotopic precursor selection setting to peptide, and MS/MS was performed on charged species of two to eight charges at a resolution of 30,000. Dynamic exclusion was set to exclude ions once within a 25-s window. All scan events occurred within a 2-s specified cycle time. The MS analysis was performed at The Herbert Wertheim UF Scripps Institute for Biomedical Innovation & Technology, Mass Spectrometry and Proteomics Core Facility (RRID:SCR_023576).

Database searching

MS/MS data were analyzed using Sequest (Thermo Fisher Scientific, San Jose, CA, USA) within Proteome Discoverer version 2.5.0.400. The Sequest was set up to search the PD_Contaminants_2015_5.fasta and UniProt Mouse filtered proteome (UP000000589, *Mus musculus*, 54,646 entries), assuming trypsin as the digestion enzyme. Search parameters included a fragment ion mass tolerance of 0.020 Da and a parent ion tolerance of 10 parts per million. Carbamidomethylation of cysteine was set as a fixed modification, while oxidation of methionine, and deamidation of asparagine were considered variable modifications.

Criteria for protein identification

Scaffold (version 5.2.0; Proteome Software Inc., Portland, OR) was used to validate peptide and protein identifications derived from MS/MS analysis. Peptides were considered valid by setting an FDR below 1% based on Percolator's posterior error probability method (*77*), and the same FDR cut off was also used at protein level identifications (*78*). In addition, a minimum of two unique peptides were required for protein identifications. When proteins shared indistinguishable peptides and could not be confidently differentiated by MS/MS data alone, they were grouped according to the principle of parsimony. Proteins with overlapping peptide evidence were organized into clusters.

Data analysis

MS data from independent LC-MS/MS experiments (sample IDs: MS222047 aka validation experiment and MS222060 aka main proteomics experiment) were analyzed to identify proteins that interact specifically with EGFP-Rhes WT. EGFP and EGFP-Rhes C263S mutant act as negative controls to distinguish nonspecific binders. Raw data files were processed using Scaffold Viewer (Scaffold_5.2.0). Before analysis, all decoy entries, human-derived contaminants, keratins, and albumins were manually excluded.

Under the Quantify tab, Venn diagrams were generated to determine proteins uniquely associated with EGFP-Rhes WT. Only proteins identified in at least two biological independent experiments were considered for further evaluation. No quantitative analysis was performed; the focus was on qualitative identification of unique interactors.

A total of 188 high-confidence candidate unique interactors of EGFP-Rhes WT were identified. These proteins were further analyzed using the STRING database to explore potential protein-protein interaction networks. From this list, the top 10 high confidence interactors that were present in at least two independent experiments are listed.

Transfection protocol

For transfection experiments, SH-SY5Y, U-87 MG, and Q7 cells were seeded in 35-mm glass-bottom dishes or appropriate culture plates and transfected 24 hours later with the respective plasmids using Lipofectamine 2000 (Thermo Fisher Scientific, catalog no. 11668027) or polyethylenimine (PEI) (Tocris, catalog no. 7854) following the manufacturer's instructions. Cells were analyzed for EGFP expression and other downstream assays 48 hours posttransfection.

For transfection of patient-derived HD-iPSCs , transfections were performed using Lipofectamine Stem reagent protocols, which are optimized for high-efficiency delivery. Following transfection, cells were maintained in Neurobasal medium supplemented with B27, GlutaMAX. Cells were monitored for EGFP expression 24 hours postinduction and used for imaging for assays.

For protein production in Expi293 cells, GFP-RASD2 (Vector builder) plasmid and mcherry-SLC4A7 (Vector builder) were transfected to 400 ml of Expi293 cells at a ratio of 1 μg/μl using PEI (1 mg/ml) at a ratio of 1:3 for 48 hours. After incubation, the cells were pelleted at 4000 rpm for 5 min and stored at −80°C until purification.

For gene knockdown studies, Lipofectamine RNAiMAX (Thermo Fisher Scientific, catalog no. 13778030) was used to transfect U-87 MG cells with siRNA (Thermo Fisher Scientific), and cells were harvested 72 hours posttransfection for analysis. STHdh Q7/Q7 cells were transfected with siRNA using Lipofectamine 2000, and samples were collected 48 hours posttransfection for functional validation. For a 10-cm dish, we transfected ~8 μg of DNA, and for 35-mm dishes, ranging from 1 to 2 μg total DNA.

Cell viability assay

Cell viability was evaluated using the CellTiter-Glo Luminescent Cell Viability Assay (Promega, G7573). U-87 cells were plated in 96-well plates and transfected with EGFP, EGFP-Rhes, or EGFP-Rhes-C263S constructs, or with Rhes and Slc4a7 siRNAs. At 48 hours posttransfection for the GFP constructs and 72 hours for the siRNA groups, an equal volume of CellTiter-Glo reagent was added to each well. The plate was gently mixed and incubated for 10 min at room temperature to ensure complete lysis and signal stabilization. Luminescence was recorded using a plate reader, and values were normalized to control samples to calculate relative cell viability.

Quantitative real-time PCR

qPCR was performed to assess the knockdown efficiency of SLC4A7 and RASD2 in U-87 MG cells. Total RNA was isolated using TRIzol-based method, and cDNA was synthesized using cDNA synthesis qScript Ultra Supermix (Quanta Bio, catalog no. 95217-025) according to the manufacturer's instructions.

Real-time PCR was carried out using the PowerUp SYBR Green Master Mix (Applied Biosystems, catalog no. A25742) on a QuantStudio 3 real-time PCR machine. Each reaction was run in technical triplicates, and data were normalized to human GAPDH expression as the endogenous control. Relative expression levels were calculated using the ΔCt method. Data are represented as fold change relative to control conditions.

Inhibitor treatment

U-87 MG and /Q7 cells expressing EGFP-Rhes were treated with DIDS (Sigma-Aldrich, catalog no. 309795-250MG) at final concentrations of 10, 100, 250 μM and 500 μM. Treatments were performed for 4 to 5 hours at 37°C for U-87 MG and 33°C for Q7 striatal neuronal cells in a humidified incubator.

To assess the effect of farnesylation inhibition on TNT formation and Rhes-Slc4a7 interaction, Q7 striatal neuronal cells were treated with Lonafarnib (Sigma-Aldrich, catalog no. SML1457-5MG) at four different concentrations 5, 10, 20, and 100 μM for 24 hours. dimethyl sulfoxide (DMSO)–treated cells served as controls. Live-cell imaging was performed using a Zeiss LSM 990 confocal microscope to visualize TNT-like structures. In addition, co-IP assays were conducted post-treatment to examine Rhes-Slc4a7 binding. Cell lysates were subjected to IP using GST beads, followed by immunoblotting to detect interacting proteins.

Intracellular pH assay measurement using SEpHluorin

Intracellular pH calibration was carried out using the Intracellular pH Calibration Buffer Kit (Thermo Fisher Scientific, catalog no. P35379). U-87 cells were transfected with the Lyn-mCherry-SEpHluorin construct and imaged 48 hours posttransfection. Cells were treated with calibration buffers of known pH values (4.5, 5.5, 6.5, and 7.5) containing nigericin and valinomycin to equalize intracellular and extracellular pH, as recommended by the manufacturer's protocol. Confocal imaging was performed using a Zeiss LSM 990 microscope, and the SEpHluorin (GFP channel) to mCherry fluorescence ratio at the cell cortex was determined for each pH condition to generate a standard calibration curve.

To assess changes in intracellular pH upon Slc4a7 knockdown or inhibition by DIDS in presence and absence of Rhes, U-87 or Q7 cells were transfected with the pH sensor construct Lyn-tailed mCherry-SEpHluorin (Addgene plasmid #32002) gifted to us by S. Falsig Pedersen (University of Copenhagen), which encodes a membrane-targeted dual-fluorophore fusion protein. This construct combines mCherry (a pH-insensitive red fluorophore) and super ecliptic pHluorin (SEpHluorin), a pH-sensitive GFP variant whose fluorescence decreases under acidic conditions.

To measure intracellular pH changes in U-87 cells upon Slc4a7 depletion, cells were first transfected with control or Slc4a7-specific siRNAs. Twenty-four hours postcotransfection with Lyn-mCherry-SEpHluorin and either BFP (control) or BFP-Rhes plasmids using Lipofectamine 2000. Forty hours posttransfection, cells were treated with either vehicle control (DMSO) or 100 μM DIDS for 4 to 5 hours.

At 48 hours posttransfection, confocal imaging was performed using Olympus FV3000 with a 63× oil immersion objective. For quantification, integrated fluorescence intensity of both GFP (SEpHluorin) and mCherry at the plasma membrane was measured using ImageJ. The GFP/mCherry fluorescence ratio was calculated for each cell, with mCherry serving as an internal normalization control.

Quantification was performed on 30 cells per condition, averaged across three independent experiments. Reduced GFP/mCherry ratios were interpreted as indicative of intracellular acidification.

Cellular imaging protocol

To visualize the actin cytoskeleton in U-87 MG cells, Alexa Fluor 647 Phalloidin (Thermo Fisher Scientific, catalog no. A30107) was used at a 1:400 dilution. Fixation was performed using a protocol optimized to preserve TNTs (*79*). Cells were first fixed in 4% paraformaldehyde (PFA; Electron Microscopy Sciences, catalog no. 15714) with 0.2 M HEPES (Thermo Fisher Scientific, catalog no. CAS 7365-45-9) in PBS for 15 min, followed by a second fixation in 5 mM dithiobispropionimidate (Thermo Fisher Scientific, catalog no. PI20665) with 25 mM Hepes for another 15 min.

After fixation, cells were permeabilized using 0.1% Triton X-100 in PBS for min, washed, and incubated in blocking buffer (5% normal horse serum in PBS-Tween with 1% bovine serum albumin) for 1 hour at room temperature. Phalloidin staining was carried out overnight at 4°C in a humidified chamber. Coverslips were washed and mounted with antifade mounting medium (stored at 4°C).

To visualize Halo-Rhes for STED imaging, Q7 striatal cells transiently expressing Halo-Rhes, and GFP-Slc4a7 constructs were incubated with Janelia Fluor 646 HaloTag ligand (catalog no. HT106A, Promega) at a dilution of 1:400. The ligand was added directly to the culture medium, and cells were incubated for 1 hour at 33°C . Following incubation, cells were washed twice with 1× PBS to remove unbound ligand and were immediately taken for imaging. For live-cell imaging, DMEM was replaced with live-cell imaging solution (Invitrogen, catalog no. A14291DJ).

To visualize the plasma membrane, cells were stained with wheat germ agglutinin (WGA) conjugated to Alexa Fluor 647 (Thermo Fisher Scientific, catalog no. W32466). Live cells were incubated with WGA (0.5 μg/ml in culture medium) for 5 min at room temperature, gently washed with PBS to remove unbound dye, and immediately imaged using a Zeiss LSM 990 confocal microscope.

IP and immunoblotting

For co-IP assays, Q7 striatal cell lysates were prepared using IP lysis buffer [50 mM tris (pH 7.8), 150 mM NaCl, 10% glycerol, 1% Triton X-100 with protease inhibitor, and phosphatase inhibitors]. To assess protein-protein interactions, GFP pull-down was performed using GFP-Trap agarose beads (Chromotek), and GST pull-down was done using glutathione Sepharose beads (GE Healthcare). Lysates were incubated with beads overnight at 4°C with gentle rotation. After incubation, beads were washed thoroughly with wash buffer [50 mM tris (pH 7.8), 150 mM NaCl, 10% glycerol, and 1% Triton X-100], and bound proteins were eluted using 2× LDS sample buffer supplemented with β-ME and boiled at 95°C for 5 min.

For immunoblotting, protein samples were loaded on SDS–polyacrylamide gel electrophoresis and transferred onto a polyvinylidene difluoride membrane. Membranes were incubated with specific primary antibodies (at 4°C overnight), followed by secondary antibodies (at room temperature for 1 hour). The antibodies used were anti-Slc4a7 (Invitrogen, catalog no. PA5-75807, 1: 2000), anti-GAPDH (Santa Cruz Biotechnology, catalog no. SC-32233, 1: 5000), anti-GST (Santa Cruz Biotechnology, SC-138, 1:5000), anti-GFP (Santa Cruz Biotechnology, catalog no. SC-9993), anti-Myc (Santa Cruz Biotechnology, catalog no. SC-40-9E10, 1:5000), anti-actin (Santa Cruz Biotechnology, catalog no. SC-47778, 1:10,000), anti-mouse immunoglobulin G–horseradish peroxidase (IgG-HRP, the Jackson Laboratory, 1:10,000), and anti-rabbit IgG-HRP (the Jackson Laboratory, 1:10,000). Protein bands were visualized using enhanced chemiluminescence reagents and detected using the Azure Biosystems imaging system.

Flow cytometry

We conducted FACS-based assays to study mHTT intercellular transfer via Rhes-TNTs and to test whether TNTs are open-ended structures for cytosolic exchange. To prepare FACS samples, cells were harvested 48 hours posttransfection, trypsinized, and resuspended in FACS buffer containing 25 mM HEPES, deoxyribonuclease I (10 U/ml), 5 mM EDTA, and 2% FBS in Ca^{2+}/Mg^{2+}-free Dulbecco's phosphate-buffered saline (DPBS). Single-cell suspensions were filtered through 40-μm nylon mesh and sorted using a FACSAria sorter (BD Biosciences). Sorted cells were cocultured at 1:1 ratio in 12-well plates for 24 hours. Following coculture, the cells were trypsinized, washed in DPBS, and analyzed using BD LSR Fortessa flow cytometer. Data were compensated using single-color controls and analyzed using FlowJo software.

In TNT-mediated transport assays, BFP-C1–transfected striatal cells (acceptor) were sorted after 48 hours. In parallel, donor cells were cotransfected with GFP + mCherry mHTT or GFP-Rhes + mCherry mHTT (4 μg each) in two 10-cm dishes for each, sorted as double-positive cells, and cocultured with BFP^+ cells for 24 hours. Transfer of tagged proteins into BFP^+ cells was analyzed by gating for GFP/mCherry signal in the BFP^+ population.

To assess open-ended TNTs, we used split-GFP constructs. Q7 cells were transfected with CD63-7G11-IRES-CFP and G10-IRES-mCherry in two 10-cm dishes for each. Preculture mixtures showed no GFP fluorescence, confirming the absence of self-assembly. Following FACS based on CFP and mCherry expression, the cells were cocultured. After 24 hours, the cells were analyzed by gating on BFP^+ cells for GFP signal, which indicated functional cytosolic exchange via open-ended TNTs.

BRET assay

To assess the interaction between Rhes and Slc4a7, we performed a NanoBRET assay (Promega) based on energy transfer between a bioluminescent donor and a fluorescent acceptor when in close proximity (<10 nm). Human RHES was fused at its N terminus to HaloTag, and human SLC4A7 was fused at its N terminus to the NanoLuciferase. Constructs were cloned into mammalian expression vectors under the control of a EF1 promoter (Vector builder). The HaloTag was labeled with the HaloTag 618 ligand (Promega, catalog no. G9801) to serve as fluorescent acceptor. Striatal neuronal were maintained in DMEM (Gibco) supplemented with 10% FBS and 1% penicillin-streptomycin at 33°C in a humidified atmosphere with 5% CO_2. For BRET assays, cells were plated in 96-well white opaque-bottom plates (Thermo Fisher Scientific, catalog no. 15052) at a density of 2×10^4 cells per well. After 16 hours, cells were cotransfected with 50 ng of Halo-Rhes and 50 ng of NLuc-SLC4A7-NLuc plasmids in Opti-MEM (Thermo Fisher Scientific, catalog no. 31985062) using PEI transfection reagent (1:3 ratio). Control cells received only donor or acceptor constructs as needed. At 24 hours posttransfection, the cells were added with DMSO (0.1%) or with HaloTag 618 ligand (1:500, Promega) for overnight at 33°C, followed by two washes with PBS, and incubation NLuc substrate furimazine (Promega, catalog no. N113A) was added at a final concentration

of 10 μM, and BRET measurements were taken within 10 min using a microplate reader (Flexistation 3, Molecular probes). Emission signals were collected at 460 nm (donor) and 618 nm (acceptor). The BRET ratio was calculated as the intensity of the acceptor emission (618 nm) divided by the donor emission (460 nm), after subtraction of background signal from donor-only transfected cells. BRET curves were generated by plotting the BRET ratio versus the acceptor/donor expression ratio (estimated from fluorescence and luminescence intensities, respectively) comparing DMSO and Halo-Tag–treated cells. Data were plotting using GraphPad Prism software.

Protein purification, in vitro interaction, and striatal Rhes binding

Protein purification from Expi293 cells was carried out by dissolving the pellet in the ice-cold lysis buffer [50 mM tris (pH 7.8), 150 mM NaCl, 10% glycerol, and 1% Triton X-100 with protease inhibitor cocktail] followed by sonication of samples for 4 min (5 s on and 10 s off) and centrifuged at 18,000 rpm for 1 hour. The supernatant was bound to GFP nano beads and HA nano beads for RASD2 and SLC4A7, respectively, overnight at 4°C and the beads were washed three times for 30 min with the wash buffer [50 mM tris (pH 7.8), 150 mM NaCl, 10% glycerol, and 1% Triton X-100]. After washing, the cleavage was done with precision protease overnight. Next day, the precision protease was removed after binding with glutathione resin for 4 hours, centrifuged at 2500 rpm for 5 min, and the supernatant contains the cleaved protein.

For the in vitro–binding assay, an equimolar concentration of recombinant purified SLC4A7 was incubated with EGFP Rhes overnight at 4°C and SLC4A7 was detected by Western blotting with SLC4A7 antibody (1:2000 Invitrogen). The control for the experiment was GFP nanobead incubated with cleaved SLC4A7. The input was cleaved SLC4A7 protein.

To examine the interaction between Slc4a7 and striatal Rhes, striatal lysates from WT mice were prepared in tris IP buffer [50 mM tris (pH 7.8), 150 mM NaCl, 1% Triton X-100, and 10% glycerol] containing protease and phosphatase inhibitors. Each reaction contained 0.2 mg of lysate, 10 μg of purified HA-Slc4a7, and 15 μl of HA nanobeads in a total volume of 1 ml, incubated at 4°C overnight. The complexes were then washed three times with tris IP buffer (without inhibitors) and eluted using 25 μl of 2× LDS buffer. As a control, lysates were incubated with HA nanobeads alone under identical conditions, without the addition of purified HA-Slc4a7.

Confocal and STED imaging and analysis

All fluorescent confocal images were acquired using either an Olympus FV3000 or a Zeiss LSM 990 confocal microscope equipped with a 63× oil immersion objective [numerical aperture (NA) 1.4]. Fluorophores were excited using a 488-nm argon ion laser (for GFP channel) and a 633-nm diode-pumped solid-state laser (for far-red fluorophore). TNT-like protrusions were imaged using a Z-step size of 0.27 μm, optimized to capture the entire three-dimensional (3D) cellular volume. Image processing for datasets acquired on the Zeiss 990 was performed using ZEN Black, while images from the Olympus FV3000 were processed using FV31S-DT software. For TNT quantification, only protrusions that directly connected two distinct cells and were above the substratum were counted.

TNTs were identified in confocal images acquired using either a Zeiss LSM 990 or Olympus FV3000 microscope. Structures were classified as TNTs only if they were (i) suspended above the substratum, (ii) clearly connecting two cells, and (iii) within a diameter range of 150 to 300 nm. Image z-stacks were analyzed using ZEN Blue or FV31S-DT software to confirm that the structures were not attached to the culture surface. TNT length (defined as the distance between connected cells) and diameter (measured at the midpoint) were quantified using the line measurement tool in ZEN Blue. Multiple TNTs were analyzed per field across independent experiments, with at least 50 TNTs measured per group.

STED images were acquired with an Abberior microscope controlled by Imspector software (Abberior Instruments). STED laser lines 488 and 640 nm were used for excitation. Cells were imaged with a 60× NA = 1.4 P-Apo oil objective. Imspector software was used to analyze STED images and to calculate FWHM values.

Time-lapse fluorescence imaging was performed using a Zeiss LSM 990 Airyscan microscope with a 63×/1.4 NA oil DIC M27 objective. Cells were kept in live-cell imaging solution (Life technologies, catalog no. A59688DJ) and maintained in a 35-mm glass-bottom dish within a live-cell environmental chamber at 33°C, 5% CO_2, and 80% humidity. Excitation lasers at 488, 561, and 639 nm were used, with images acquired every 2 min. A Z-step size of 150.6 nm was used to capture regions above and below the TNTs without imaging below the substratum. Image processing, including 3D Airyscan reconstruction and maximum intensity orthogonal projections, was performed using Zeiss Zen Blue 3.12 software.

Colocalization analysis

Colocalization analysis was performed using ZEN Blue software (Zeiss LSM 990). For each image, single confocal planes were examined to assess the spatial relationship between the two fluorescent signals in defined regions. Regions of interest (ROIs) were manually selected at the TNT base, along the TNT shaft, and at the cell cortex. Pearson's correlation coefficient was calculated for each ROI to quantify the degree of signal overlap between the two fluorophores.

Stereotaxic surgery and lentiviral injection

Stereotaxic injections were performed on adult Slc4a7-KO mice (six male and six female) and WT (eight male and seven female) mice (8 to 10 weeks old). Animals were housed in groups of three to five under a 12-hour light/dark cycle with unrestricted access to food and water. All procedures complied with the 3R principles (replacement, reduction, and refinement) and were approved by the Institutional Animal Care and Use Committee at The Herbert Wertheim UF Scripps Institute, Florida (IACUC number: 15-019). Intrastriatal delivery of lentivirus was carried out using established stereotaxic coordinates from prior studies (*11*). During surgery, mice were anesthetized with isoflurane delivered in oxygen and secured in a stereotaxic apparatus (David Kopf Instruments). A unilateral injection into the striatum was performed at coordinates as follows: Mediolateral ±1.6 mm, Anteroposterior +1.0 mm, and Dorsoventral −3.6 mm relative to bregma. A total volume of 0.5 μl of virus was infused. The lentivirus used was GFP-P2A-mCherry HTT N171-89Q (nine for WT and seven for KO, mixed sex) at a concentration of 1.0×10^{12} gc/ml, or GFP-P2A-mCherry HTTN171-18Q (six for WT and five for KO, mixed sex) at a concentration of 1.0×10^{12} gc/ml.

Tissue fixation and preparation for imaging

To preserve endogenous fluorescence, tissue was processed with minimal handling. Eight weeks post–stereotaxic injection, mice were deeply anesthetized and transcardially perfused with 10 ml of

ice-cold saline at a flow rate of 1.5 ml/min, followed by 10 ml of 4% PFA at the same rate. Brains were harvested and postfixed overnight in 4% PFA at 4°C and then cryoprotected using a sucrose gradient (10, 20, and 30% in PBS). Tissues were embedded in Tissue-Tek OCT compound (Sakura) and sectioned coronally at 20-µm thickness. Sections were mounted on Superfrost/Plus slides, counterstained with DAPI, and coverslipped using Fluoromount-G (Thermo Fisher Scientific). Imaging was performed using a Zeiss LSM 880 confocal microscope, and images were processed using ZEN software (Zeiss).

Statistical analysis

Data are presented as means ± SEM as indicated in figure legends. All experiments were performed at least three times. The statistical comparison was performed between groups using one-way analysis of variance (ANOVA), two-way ANOVA, and Student's *t* test as indicated in figure legends, and significance values were set at $P < 0.05$, using Graph Pad Prism9.

Supplementary Materials

This PDF file includes:

Figs. S1 to S8
Legend for movie S1
Legend for dataset S1

Other Supplementary Material for this manuscript includes the following:

Movie S1
Dataset S1

REFERENCES

1. C. Zurzolo, Tunneling nanotubes: Reshaping connectivity. *Curr. Opin. Cell Biol.* **71**, 139–147 (2021).
2. S. Subramaniam, Striatal induction and spread of the Huntington's disease protein: A novel Rhes route. *J. Huntingtons Dis.* **11**, 281–290 (2022).
3. S. Nath, L. Agholme, F. R. Kurudenkandy, B. Granseth, J. Marcusson, M. Hallbeck, Spreading of neurodegenerative pathology via neuron-to-neuron transmission of β-amyloid. *J. Neurosci.* **32**, 8767–8777 (2012).
4. M. Chang, S. Krussel, L. K. Parajuli, J. Kim, D. Lee, A. Merodio, J. Kwon, S. Okabe, H.-B. Kwon, Intercellular communication in the brain through a dendritic nanotubular network. *Science* **390**, eadr7403 (2025).
5. H. Scheiblich, F. Eikens, L. Wischhof, S. Opitz, K. Jüngling, C. Cserép, S. V. Schmidt, J. Lambertz, T. Bellande, B. Pósfai, C. Geck, J. Spitzer, A. Odainic, S. Castro-Gomez, S. Schwartz, I. Boussaad, R. Krüger, E. Glaab, D. A. DiMonte, D. Bano, Á. Dénes, E. Latz, R. Melki, H.-C. Pape, M. T. Heneka, Microglia rescue neurons from aggregate-induced neuronal dysfunction and death through tunneling nanotubes. *Neuron* **112**, 3106–3125.e8 (2024).
6. R. Chakraborty, T. Nonaka, M. Hasegawa, C. Zurzolo, Tunnelling nanotubes between neuronal and microglial cells allow bi-directional transfer of α-Synuclein and mitochondria. *Cell Death Dis.* **14**, 329 (2023).
7. K. Eltom, T. Mothes, S. Libard, M. Ingelsson, A. Erlandsson, Astrocytic accumulation of tau fibrils isolated from Alzheimer's disease brains induces inflammation, cell-to-cell propagation and neuronal impairment. *Acta Neuropathol. Commun.* **12**, 34 (2024).
8. S. Subramaniam, Rhes tunnels: A radical new way of communication in the brain's striatum? *Bioessays* **42**, e1900231 (2020).
9. S. Subramaniam, S. H. Snyder, Huntington's disease is a disorder of the corpus striatum: Focus on Rhes (Ras homologue enriched in the striatum). *Neuropharmacology* **60**, 1187–1192 (2011).
10. M. Sharma, S. Subramaniam, Rhes travels from cell to cell and transports Huntington disease protein via TNT-like protrusion. *J. Cell Biol.* **218**, 1972–1993 (2019).
11. U. N. Ramirez-Jarquin, M. Sharma, N. Shahani, Y. Li, S. Boregowda, S. Subramaniam, Rhes protein transits from neuron to neuron and facilitates mutant huntingtin spreading in the brain. *Sci. Adv.* **8**, eabm3877 (2022).
12. E. Boedtkjer, C. Aalkjaer, Intracellular pH in the resistance vasculature: Regulation and functional implications. *J. Vasc. Res.* **49**, 479–496 (2012).
13. S. H. F. Pedersen, Acid-base transporters in the context of tumor heterogeneity. *Pflugers Arch.* **476**, 689–701 (2024).
14. I. Choi, K. Beedholm, V. S. Dam, S. H. Bae, D. J. Noble, S. M. Garraway, C. Aalkjaer, E. Boedtkjer, Sodium bicarbonate cotransporter NBCn1/Slc4a7 affects locomotor activity and hearing in mice. *Behav. Brain Res.* **401**, 113065 (2021).
15. Y. Zhuang, D. Li, C. Tang, X. Zhao, R. Wang, D. Tao, X. Huang, X. Liu, *Slc4a7* regulates retina development in zebrafish. *Int. J. Mol. Sci.* **25**, 9613 (2024).
16. M. Jiang, A. Salari, C. Stock, K. Nikolovska, E. Boedtkjer, M. Amiri, U. E. Seidler, The electroneutral Na^+–HCO_3^- cotransporter NBCn1 (SLC4A7) modulates colonic enterocyte pH_i, proliferation, and migration. *Am. J. Physiol. Cell Physiol.* **326**, C1625–C1636 (2024).
17. T. Cerbini, R. Funahashi, Y. Luo, C. Liu, K. Park, M. Rao, N. Malik, J. Zou, Transcription activator-like effector nuclease (TALEN)-mediated CLYBL targeting enables enhanced transgene expression and one-step generation of dual reporter human induced pluripotent stem cell (iPSC) and neural stem cell (NSC) lines. *PLOS ONE* **10**, e0116032 (2015).
18. C. Zhang, R. Schekman, Syncytin-mediated open-ended membrane tubular connections facilitate the intercellular transfer of cargos including Cas9 protein. *eLife* **12**, e84391 (2023).
19. H. Shinomiya, Plastin family of actin-bundling proteins: Its functions in leukocytes, neurons, intestines, and cancer. *Int. J. Cell Biol.* **2012**, 213492 (2012).
20. A. W. Peng, I. A. Belyantseva, P. D. Hsu, T. B. Friedman, S. Heller, Twinfilin 2 regulates actin filament lengths in cochlear stereocilia. *J. Neurosci.* **29**, 15083–15088 (2009).
21. L. Muller, R. Keil, M. Glaß, M. Hatzfeld, Plakophilin 4 controls the spatio-temporal activity of RhoA at adherens junctions to promote cortical actin ring formation and tissue tension. *Cell. Mol. Life Sci.* **81**, 291 (2024).
22. J. M. Henderson, N. Ljubojevic, S. Belian, T. Chaze, D. Castaneda, A. Battistella, Q. Giai Gianetto, M. Matondo, S. Descroix, P. Bassereau, C. Zurzolo, Tunnelling nanotube formation is driven by Eps8/IRSp53-dependent linear actin polymerization. *EMBO J.* **42**, e113761 (2023).
23. N. Y. Yang, T. Mukaibo, I. Kurtz, J. E. Melvin, The apical Na^+ –HCO_3^- cotransporter Slc4a7 (NBCn1) does not contribute to bicarbonate transport by mouse salivary gland ducts. *J. Cell. Physiol.* **234**, 16376–16388 (2019).
24. E. Boedtkjer, J. Praetorius, C. Aalkjaer, NBCn1 (slc4a7) mediates the Na^+–dependent bicarbonate transport important for regulation of intracellular pH in mouse vascular smooth muscle cells. *Circ. Res.* **98**, 515–523 (2006).
25. S. Valdebenito, S. Malik, R. Luu, O. Loudig, M. Mitchell, G. Okafo, K. Bhat, B. Prideaux, E. A. Eugenin, Tunneling nanotubes, TNT, communicate glioblastoma with surrounding non-tumor astrocytes to adapt them to hypoxic and metabolic tumor conditions. *Sci. Rep.* **11**, 14556 (2021).
26. B.-R. Choi, S. Bang, Y. Chen, J. H. Cheah, S. F. Kim, PKA modulates iron trafficking in the striatum via small GTPase, Rhes. *Neuroscience* **253**, 214–220 (2013).
27. W. Wang, K. Tsirulnikov, H. R. Zhekova, G. Kayik, H. M. Khan, R. Azimov, N. Abuladze, L. Kao, D. Newman, S. Y. Noskov, Z. H. Zhou, A. Pushkin, I. Kurtz, Cryo-EM structure of the sodium-driven chloride/bicarbonate exchanger NDCBE. *Nat. Commun.* **12**, 5690 (2021).
28. M. Koivusalo, C. Welch, H. Hayashi, C. C. Scott, M. Kim, T. Alexander, N. Touret, K. M. Hahn, S. Grinstein, Amiloride inhibits macropinocytosis by lowering submembranous pH and preventing Rac1 and Cdc42 signaling. *J. Cell Biol.* **188**, 547–563 (2010).
29. V. Middel, L. Zhou, M. Takamiya, T. Beil, M. Shahid, U. Roostalu, C. Grabher, S. Rastegar, M. Reischl, G. U. Nienhaus, U. Strahle, Dysferlin-mediated phosphatidylserine sorting engages macrophages in sarcolemma repair. *Nat. Commun.* **7**, 12875 (2016).
30. O. Ilnytska, M. Jeziorek, K. Lai, N. Altan-Bonnet, R. Dobrowolski, J. Storch, Lysobisphosphatidic acid (LBPA) enrichment promotes cholesterol egress via exosomes in Niemann Pick type C1 deficient cells. *Biochim. Biophys. Acta Mol. Cell Biol. Lipids* **1866**, 158916 (2021).
31. R. Y. Chan, T. T. Loh, Perturbation of intracellular pH by DIDS on endocytosis of transferrin and iron uptake in rabbit reticulocytes. *Biochem. Biophys. Res. Commun.* **150**, 1256–1262 (1988).
32. H. Wioland, A. Jegou, G. Romet-Lemonne, Quantitative variations with pH of actin depolymerizing factor/Cofilin's multiple actions on actin filaments. *Biochemistry* **58**, 40–47 (2019).
33. N. Yonezawa, E. Nishida, H. Sakai, pH control of actin polymerization by cofilin. *J. Biol. Chem.* **260**, 14410–14412 (1985).
34. L. Blondin, V. Sapountzi, S. K. Maciver, E. Lagarrigue, Y. Benyamin, C. Roustan, A structural basis for the pH-dependence of cofilin. F-actin interactions. *Eur. J. Biochem.* **269**, 4194–4201 (2002).
35. H. H. Damkier, S. Nielsen, J. Praetorius, Molecular expression of SLC4-derived Na^+–dependent anion transporters in selected human tissues. *Am. J. Physiol. Regul. Integr. Comp. Physiol.* **293**, R2136–R2146 (2007).
36. H. J. Park, I. Rajbhandari, H. S. Yang, S. Lee, D. Cucoranu, D. S. Cooper, J. D. Klein, J. M. Sands, I. Choi, Neuronal expression of sodium/bicarbonate cotransporter NBCn1 (SLC4A7) and its response to chronic metabolic acidosis. *Am. J. Physiol. Cell Physiol.* **298**, C1018–C1028 (2010).
37. D. Spano, I. Branchi, A. Rosica, M. T. Pirro, A. Riccio, P. Mithbaokar, A. Affuso, C. Arra, P. Campolongo, D. Terracciano, V. Macchia, J. Bernal, E. Alleva, R. Di Lauro, Rhes is involved in striatal function. *Mol. Cell. Biol.* **24**, 5788–5796 (2004).
38. D. Bok, G. Galbraith, I. Lopez, M. Woodruff, S. Nusinowitz, H. BeltrandelRio, W. Huang, S. Zhao, R. Geske, C. Montgomery, I. Van Sligtenhorst, C. Friddle, K. Platt, M. J. Sparks,

A. Pushkin, N. Abuladze, A. Ishiyama, R. Dukkipati, W. Liu, I. Kurtz, Blindness and auditory impairment caused by loss of the sodium bicarbonate cotransporter NBC3. *Nat. Genet.* **34**, 313–319 (2003).
39. I. A. Lopez, D. Acuna, G. Galbraith, D. Bok, A. Ishiyama, W. Liu, I. Kurtz, Time course of auditory impairment in mice lacking the electroneutral sodium bicarbonate cotransporter NBC3 (slc4a7). *Brain Res. Dev. Brain Res.* **160**, 63–77 (2005).
40. D. S. Williams, Usher syndrome: Animal models, retinal function of Usher proteins, and prospects for gene therapy. *Vision Res.* **48**, 433–441 (2008).
41. H. Ishiguro, D. Walther, T. Arinami, G. R. Uhl, Variation in a bicarbonate co-transporter gene family member SLC4A7 is associated with propensity to addictions: A study using fine-mapping and three samples. *Addiction* **102**, 1320–1325 (2007).
42. J. R. Schank, S. Lee, C. E. Gonzalez-Islas, S. E. Nennig, H. D. Fulenwider, J. Chang, J. M. Li, Y. Kim, L. A. Jeffers, J. Chung, J.-K. Lee, Z. Jin, C. Aalkjaer, E. Boedtkjer, I. Choi, Increased alcohol consumption in mice lacking sodium bicarbonate transporter NBCn1. *Sci. Rep.* **10**, 11017 (2020).
43. F. Napolitano, A. De Rosa, R. Russo, A. Di Maio, M. Garofalo, M. Federici, S. Migliarini, A. Ledonne, F. R. Rizzo, L. Avallone, T. Nuzzo, T. Biagini, M. Pasqualetti, N. B. Mercuri, T. Mazza, A. Chambery, A. Usiello, The striatal-enriched protein Rhes is a critical modulator of cocaine-induced molecular and behavioral responses. *Sci. Rep.* **9**, 15294 (2019).
44. G. C. Quintero, D. Spano, Exploration of sex differences in Rhes effects in dopamine mediated behaviors. *Neuropsychiatr. Dis. Treat.* **7**, 697–706 (2011).
45. D. S. Cooper, H. S. Yang, P. He, E. Kim, I. Rajbhandari, C. C. Yun, I. Choi, Sodium/bicarbonate cotransporter NBCn1/slc4a7 increases cytotoxicity in magnesium depletion in primary cultures of hippocampal neurons. *Eur. J. Neurosci.* **29**, 437–446 (2009).
46. H. J. Park, C. E. Gonzalez-Islas, Y. Kang, J. M. Li, I. Choi, Deletion of the Na/HCO3 transporter NBCn1 protects hippocampal neurons from NMDA-induced seizures and neurotoxicity in Mice. *Sci. Rep.* **9**, 15981 (2019).
47. S. Okamoto, M. A. Pouladi, M. Talantova, D. Yao, P. Xia, D. E. Ehrnhoefer, R. Zaidi, A. Clemente, M. Kaul, R. K. Graham, D. Zhang, H. S. Vincent Chen, G. Tong, M. R. Hayden, S. A. Lipton, Balance between synaptic versus extrasynaptic NMDA receptor activity influences inclusions and neurotoxicity of mutant huntingtin. *Nat. Med.* **15**, 1407–1413 (2009).
48. S. Swarnkar, Y. Chen, W. M. Pryor, N. Shahani, D. T. Page, S. Subramaniam, Ectopic expression of the striatal-enriched GTPase Rhes elicits cerebellar degeneration and an ataxia phenotype in Huntington's disease. *Neurobiol. Dis.* **82**, 66–77 (2015).
49. N. S. Jennifer Hernandez, S. Swarnkar, S. Subramaniam, Rhes deletion prevents age-dependent selective motor deficits and reduces phosphorylation of S6K in Huntington disease Hdh150Q(CAG) knock-in mice. BioRxiv. 2021.06.16.448681 [Preprint] (2021).
50. E. Boedtkjer, J. M. Moreira, M. Mele, P. Vahl, V. T. Wielenga, P. M. Christiansen, V. E. Jensen, S. F. Pedersen, C. Aalkjaer, Contribution of Na^+,HCO_3^--cotransport to cellular pH control in human breast cancer: A role for the breast cancer susceptibility locus NBCn1 (SLC4A7). *Int. J. Cancer* **132**, 1288–1299 (2013).
51. A. Gorbatenko, C. W. Olesen, N. Morup, G. Thiel, T. Kallunki, E. Valen, S. F. Pedersen, ErbB2 upregulates the Na^+,HCO_3^--cotransporter NBCn1/*SLC4A7* in human breast cancer cells via Akt, ERK, Src, and Kruppel-like factor 4. *FASEB J.* **28**, 350–363 (2014).
52. S. Lee, T. V. Axelsen, A. P. Andersen, P. Vahl, S. F. Pedersen, E. Boedtkjer, Disrupting Na^+, HCO_3^--cotransporter NBCn1 (Slc4a7) delays murine breast cancer development. *Oncogene* **35**, 2112–2122 (2016).
53. S. Lee, T. V. Axelsen, N. Jessen, S. F. Pedersen, P. Vahl, E. Boedtkjer, Na^+,HCO_3^--cotransporter NBCn1 (Slc4a7) accelerates ErbB2-induced breast cancer development and tumor growth in mice. *Oncogene* **37**, 5569–5584 (2018).
54. X. Y. Li, J.-P. Sun, H. Guo, X.-Q. Fan, S.-S. Zhang, B. Wang, N. Yu, Q.-H. Li, Modulation of RASD2 by miRNA-485-5p drives thyroid cancer progression and metastasis. *Kaohsiung J. Med. Sci.* **41**, e70028 (2025).
55. M. Xie, C. Xin, RASD2 promotes the development and metastasis of uveal melanoma via enhancing glycolysis. *Biochem. Biophys. Res. Commun.* **610**, 92–98 (2022).
56. S. Subramaniam, F. Napolitano, R. G. Mealer, S. Kim, F. Errico, R. Barrow, N. Shahani, R. Tyagi, S. H. Snyder, A. Usiello, Rhes, a striatal-enriched small G protein, mediates mTOR signaling and L-DOPA-induced dyskinesia. *Nat. Neurosci.* **15**, 191–193 (2011).
57. E. S. Ali, A. Lipońska, B. P. O'Hara, D. R. Amici, M. D. Torno, P. Gao, J. M. Asara, M.-N. F. Yap, M. L. Mendillo, I. Ben-Sahra, The mTORC1-SLC4A7 axis stimulates bicarbonate import to enhance de novo nucleotide synthesis. *Mol. Cell* **82**, 3284–3298.e7 (2022).
58. S. Valdebenito, E. Lou, J. Baldoni, G. Okafo, E. Eugenin, The novel roles of connexin channels and tunneling nanotubes in cancer pathogenesis. *Int. J. Mol. Sci.* **19**, 1270 (2018).
59. G. Wu, J. J. Weiter, S. Santos, L. Ginsburg, R. Villalobos, The macular photostress test in diabetic retinopathy and age-related macular degeneration. *Arch. Ophthalmol.* **108**, 1556–1558 (1990).
60. G. Pinto, C. Brou, C. Zurzolo, Tunneling nanotubes: The fuel of tumor progression? *Trends Cancer* **6**, 874–888 (2020).
61. L. Taiarol, B. Formicola, S. Fagioli, G. Sierri, A. D'Aloia, M. Kravicz, A. Renda, F. Viale, R. Dal Magro, M. Ceriani, F. Re, The 3.0 cell communication: New insights in the usefulness of tunneling nanotubes for glioblastoma treatment. *Cancers* **13**, 4001 (2021).
62. F. Dubois, B. Jean-Jacques, H. Roberge, M. Benard, L. Galas, D. Schapman, N. Elie, D. Goux, M. Keller, E. Maille, E. Bergot, G. Zalcman, G. Levallet, A role for RASSF1A in tunneling nanotube formation between cells through GEFH1/Rab11 pathway control. *Cell Commun. Signal* **16**, 66 (2018).
63. A. Burtey, M. Wagner, E. Hodneland, K. O. Skaftnesmo, J. Schoelermann, I. R. Mondragon, H. Espedal, A. Golebiewska, S. P. Niclou, R. Bjerkvig, T. Kogel, H. H. Gerdes, Intercellular transfer of transferrin receptor by a contact-, Rab8-dependent mechanism involving tunneling nanotubes. *FASEB J.* **29**, 4695–4712 (2015).
64. Y. Zheng, J. Li, D. Xu, L. Liu, Y. Li, J. Yi, J. Dong, D. Pang, H. Tang, Tunneling nanotubes mediate KRas transport: Inducing tumor heterogeneity and altering cellular membrane mechanical properties. *Acta Biomater.* **185**, 312–322 (2024).
65. M. Omsland, O. Bruserud, B. T. Gjertsen, V. Andresen, Tunneling nanotube (TNT) formation is downregulated by cytarabine and NF-κB inhibition in acute myeloid leukemia (AML). *Oncotarget* **8**, 7946–7963 (2017).
66. A. D'Aloia, E. Arrigoni, B. Costa, G. Berruti, E. Martegani, E. Sacco, M. Ceriani, RalGPS2 interacts with Akt and PDK1 promoting tunneling nanotubes formation in bladder cancer and kidney cells microenvironment. *Cancers* **13**, 6330 (2021).
67. L. Simone, D. L. Capobianco, F. Di Palma, E. Binda, F. G. Legnani, A. L. Vescovi, M. Svelto, F. Pisani, GFAP serves as a structural element of tunneling nanotubes between glioblastoma cells and could play a role in the intercellular transfer of mitochondria. *Front. Cell Dev. Biol.* **11**, 1221671 (2023).
68. J. S. Bjerring, Y. Khodour, E. A. Peterson, P. C. Sachs, R. D. Bruno, Intercellular mitochondrial transfer contributes to microenvironmental redirection of cancer cell fate. *FEBS J.* **292**, 2306–2322 (2025).
69. S. J. Hanna, K. McCoy-Simandle, E. Leung, A. Genna, J. Condeelis, D. Cox, Tunneling nanotubes, a novel mode of tumor cell-macrophage communication in tumor cell invasion. *J. Cell Sci.* **132**, jcs223321 (2019).
70. J. J. Lu, W. M. Yang, F. Li, W. Zhu, Z. Chen, Tunneling nanotubes mediated microRNA-155 intercellular transportation promotes bladder cancer cells' invasive and proliferative capacity. *Int. J. Nanomedicine* **14**, 9731–9743 (2019).
71. C. Bridel, J. H. M. van Gils, S. S. M. Miedema, J. J. M. Hoozemans, Y. A. L. Pijnenburg, A. B. Smit, A. J. M. Rozemuller, S. Abeln, C. E. Teunissen, Clusters of co-abundant proteins in the brain cortex associated with fronto-temporal lobar degeneration. *Alzheimer's Res. Ther.* **15**, 59 (2023).
72. L. Ghezzi, C. Cantoni, E. Rotondo, D. Galimberti, The gut microbiome-brain crosstalk in neurodegenerative diseases. *Biomedicine* **10**, 1486 (2022).
73. J. C. C. Dos Santos, M. P. P. Lima, G. A. de Castro Brito, G. S. de Barros Viana, Role of enteric glia and microbiota-gut-brain axis in parkinson disease pathogenesis. *Ageing Res. Rev.* **84**, 101812 (2023).
74. I. Hernandez, G. Luna, J. N. Rauch, S. A. Reis, M. Giroux, C. M. Karch, D. Boctor, Y. E. Sibih, N. J. Storm, A. Diaz, S. Kaushik, C. Zekanowski, A. A. Kang, C. R. Hinman, V. Cerovac, E. Guzman, H. Zhou, S. J. Haggarty, A. M. Goate, S. K. Fisher, A. M. Cuervo, K. S. Kosik, A farnesyltransferase inhibitor activates lysosomes and reduces tau pathology in mice with tauopathy. *Sci. Transl. Med.* **11**, eaat3005 (2019).
75. A. J. Ehrenberg, K. Leng, K. N. Letourneau, I. Hernandez, C. Lew, W. W. Seeley, S. Spina, B. Miller, H. Heinsen, M. Kampmann, K. S. Kosik, L. T. Grinberg, Patterns of neuronal Rhes as a novel hallmark of tauopathies. *Acta Neuropathol.* **141**, 651–666 (2021).
76. I. H. Park, N. Arora, H. Huo, N. Maherali, T. Ahfeldt, A. Shimamura, M. W. Lensch, C. Cowan, K. Hochedlinger, G. Q. Daley, Disease-specific induced pluripotent stem cells. *Cell* **134**, 877–886 (2008).
77. L. Käll, J. D. Storey, W. S. Noble, Non-parametric estimation of posterior error probabilities associated with peptides identified by tandem mass spectrometry. *Bioinformatic* **24**, 42–48 (2008).
78. A. I. Nesvizhskii, A. Keller, E. Kolker, R. Aebersold, A statistical model for identifying proteins by tandem mass spectrometry. *Anal. Chem.* **75**, 4646–4658 (2003).
79. K. Gousset, A. Gordon, S. K. Kannan, J. Tovar, A novel microproteomic approach using laser capture microdissection to study cellular protrusions. *Int. J. Mol. Sci.* **20**, 1172 (2019).

Acknowledgments: We would like to thank S. Falsig Pedersen (University of Copenhagen) for sharing GFP-Slc4a7 WT and Lyn-tailed mCherry-SEpHluorin constructs with us. We would like to thank R. Schekman for sharing split-GFP constructs with us (CD63-7G11-IRES-CFP and G10-IRES-mCherry). We would like to thank D. Weiner at the University of Florida for sharing Slc4a7 KO mice with us. We would like to thank M. Janiszewska at UF Scripps Biomedical Research Institute for sharing U-87 cell line with us. We would like to thank all the members of the laboratory for continuous support and collaborative atmosphere. We would like to thank M. Jagdev for providing HA-Slc4a7. We would like to thank G. Pierce and L. Montgomery of SNBI for the administrative support. **Funding:** This research was supported by funding from the National Institutes of Health/National Institute of Neurological Disorders and Stroke grants R21NS128564, R01NS128225, R01NS128225-S1, and R01NS138278 and laboratory institutional

funding from Stiles-Nicholson Brain Institute at the Florida Atlantic University. This study was supported by grants awarded to S. Subramaniam. **Author contributions:** S.S. conceptualized and supervised the project. S.D. performed cell culture, proteomics, immunostaining, confocal imaging, molecular cloning, RT-PCR, FACS analysis, and analyzed the data. A.F. conducted biochemical Rhes-Slc4a7 domain interaction studies. U.N.R.-J. and V.G.L.-H. carried out mouse experiments, immunohistochemistry, and confocal imaging. E.M. acquired mHTT localization and time-lapse TNT images. S.S. also performed the BRET assays. I.Z. carried out Rhes mutant and Slc4a7 binding analyses. C.M. handled Expi293 cell culture and in vitro–binding assays. N.T.U. assisted with confocal and STED imaging. G.C. and G.T. contributed to LC-MS/MS experiments. S.S. wrote the manuscript with input from S.D., U.N.R.-J., V.G.L.-H., and G.C. All the authors discussed the manuscript. **Competing interests:** The authors declare that they have no competing interests. **Data, code, materials and availability:** All data and code needed to evaluate and reproduce the results in the paper are present in the paper and/or the Supplementary Materials. This study did not generate any new materials. All proteomics datasets were submitted to ProteomeXchange via MassIVE and can be accessed at https://proteomecentral.proteomexchange.org/cgi/GetDataset?ID=PXD065528 with ID MSV000098338. Username for web access is MSV000098338_reviewer. Password is 0J57F0MDG76rfe5F.

Submitted 30 June 2025
Accepted 18 February 2026
Published 20 March 2026
10.1126/sciadv.aea1226

ScienceAdvances

Membrane-associated Rhes-Slc4a7 complex orchestrates tunneling nanotube formation and mutant Huntingtin spread

Sunayana Dagar, Alexandra Fernandez, Uri Nimrod Ramírez-Jarquín, Violeta Gisselle Lopez-Huerta, Emaad Mirza, Chinmayee Mohapatra, Isabella Zuniga, Nicolai T. Urban, Gogce Crynen, George Tsaprailis, and Srinivasa Subramaniam

Sci. Adv. **12** (12), eaea1226. DOI: 10.1126/sciadv.aea1226